# Lipid metabolism of hepatocyte-like cells supports intestinal tumor growth in *Drosophila*

Huang, K.*[1], Miao, T.*[1], Dantas, E.[3], Sanford, J.[3], Chen, Y.[1], Hu, Y.[1,2], Moon, SJ.[1], Han, M.[1,2], Wang, K.[1], Goncalves, M.[3], and Perrimon, N[1,2]

1 Department of Genetics, Blavatnik Institute, Harvard Medical School, Harvard University, Boston, MA 02115, USA
2 Howard Hughes Medical Institute, Boston, MA, USA
3 NYU Langone Health, New York, NY, USA.

^Correspondence:
Kerui Huang: Kerui_Huang@hms.harvard.edu
Norbert Perrimon: perrimon@genetics.med.harvard.edu

*Authors contribute equally

**Abstract**

Tumors require metabolic adaptations to support their rapid growth, but how they influence lipid metabolism in distant tissues remains poorly understood. Here, we uncover a novel mechanism by which gut tumors in adult flies reprogram lipid metabolism in distal hepatocyte-like cells, known as oenocytes, to promote tracheal development and tumor growth. We show that tumors secrete a PDGF/VEGF-like factor, Pvf1, that activates the TORC1-Hnf4 signaling pathway in oenocytes. This activation enhances the production of specific lipids, including very long chain fatty acids and wax esters, that are required for tracheal growth surrounding the gut tumor. Importantly, reducing expression in oenocytes of either the transcription factor *Hnf4*, or the elongase *mElo* that generates very long chain fatty acid robustly extends lifespan, suppresses tumor growth, tracheogenesis, and associated organ wasting/cachexia-like phenotypes. Further, altering the expression level of oenocyte *Hnf4* or *mElo* in control flies affects intestinal tracheogenesis. Lipoprotein-mediated lipid transport and altered oenocyte lipid metabolism drive the observed changes in tracheogenesis. Finally, we demonstrate that this regulatory pathway is conserved in mammals, as VEGF-A stimulates lipid metabolism gene expression in human hepatocytes, and lung tumor-bearing mice show increased hepatic expression of *Hnf4* and the lipid elongation gene *Elovl7*. Our findings reveal a previously unrecognized tumor-host

interaction where tumors non-autonomously reprogram distal lipid metabolism to support their growth. This study not only identifies a novel non-autonomous role of the TORC1-Hnf4 axis in lipid-mediated tumor progression but also highlights potential targets for therapeutic intervention in cancer-associated metabolic disorders.

## Introduction

Tumor growth demands a growing supply of nutrients and oxygen. The growing tumor constantly shapes its microenvironment to favor fast growth and expansion, through secreted factors and extracellular matrix [1-4]. The composition of the tumor microenvironment (TME) varies between tumor types, but the hallmarks include increased blood vessels, immune cells, stromal cells, and extracellular matrix [5]. To overcome the increasingly hypoxic and acidic environment, TME promotes angiogenesis to restore oxygen and nutrient supply. In addition to modulating the local TME, malignant cells can exert systemic effects on distant organs—including the liver, skeletal muscle, and brain—to reshape the host's metabolic pathways, ultimately promoting further tumor progression [6-10]. Liver is a metabolic center for amino acids, carbohydrates, and lipid. A key liver-specific metabolic function is the complete urea cycle (UC), which eliminates excess ammonia by converting into urea, a less toxic waste. Previous studies have identified evidence of decreased UC activity in the livers of 4T1 breast cancer bearing mice, and the plasma of children with cancer [9], demonstrating an existing interaction between tumors and the liver [11-15]. Delineating molecular pathways involving tumor-host interaction can provide novel therapeutic targets.

Lipids play a critical role in cancer progression, by serving as building blocks, energy sources and signaling molecules. It has been observed that tumor cells reprogram lipid metabolism to enhance growth, characterized by increased lipid synthesis, lipid uptake, fatty acid oxidation (FAO) and lipid storage [16]. Tumor cells also actively reshape lipid metabolism in cells from the TME through secreted signaling molecules and drive TME to favor tumor growth. For example, increased lipid uptake and FAO in regulatory T cells (Tregs), tumor-associated macrophages (TAMs) and myeloid-derived suppressor cells

65 (MDSCs), promote their immunosuppressive function [17-19]. However, whether tumor
66 cells also reshape lipid metabolism in distal organs, such as liver, which is a metabolic
67 center for lipid transport, is not known.

68 The adult *Drosophila* midgut is a powerful model for investigating tumorigenesis and
69 tumor-driven metabolic remodeling. Many genetic alterations associated with human
70 cancers induce hyperproliferation of fly intestinal stem cells (ISCs) and lead to tumor
71 formation in the midgut [20]. In particular, expression of constitutively active Yorkie
72 (yki$^{3SA}$)—the *Drosophila* homolog of human YAP1—drives gut tumor development and
73 triggers cachexia-like phenotypes, including lipid depletion, hyperglycemia, and wasting of
74 muscle and ovaries [21, 22]. Mechanistically, yki$^{3SA}$ gut tumors secrete multiple systemic
75 factors, such as the IGF-antagonizing peptide *ImpL2* [21], *PDGF- and VEGF-related factor 1*
76 *(Pvf1*) [22] and unpaired 3 (*Upd3)* , a functional ortholog of mammalian interleukin-6 (IL-6)
77 [22]. Notably, IL-6- and PDGF/VEGF-associated inflammatory programs are also broadly
78 elevated across diverse cancer models [23-26]. Together, these observations highlight
79 tumor–host organ communication as an evolutionarily conserved process and establish
80 *Drosophila* as an excellent system to dissect tumor–host interactions *in vivo*.

81 As *Drosophila* has emerged as a simple yet powerful model to study tumor-host
82 interactions [27], we use this model to better understand the reciprocal communication
83 between liver and tumor cells. The fly midgut, oenocytes, fat body and Malpighian tubules
84 are functionally equivalent to human digestive tract, hepatocytes, adipose tissue and
85 kidney, respectively [28]. Oenocytes, which are hepatocyte-like cells, are important for
86 mobilizing stored lipids during starvation and interact closely with metabolic tissues, such
87 as the fat body to regulate lipid uptake and reprocessing [29, 30]. In addition to regulating
88 lipid metabolism under nutritional deprivation, oenocytes are the major site for synthesis
89 of cuticular hydrocarbons in pterygote insects [31-33]. Adult oenocytes synthesize
90 hydrocarbons using fatty acyl-CoA precursors via reduction to fatty aldehyde and oxidative
91 decarbonylation [34, 35]. Many fatty acid synthases, elongases and desaturases expressed
92 in adult oenocytes produce various types of fatty acyl-CoA substrates that are processed to
93 form a complex blend of cuticular hydrocarbons [36-39]. Hepatocyte nuclear factor 4

94 (Hnf4), an oenocyte enriched transcription factor, plays an important role in regulating the
95 conversion of lipids to very long chain fatty acid, which are important substrates for
96 hydrocarbon synthesis [39]. Oenocytes are the major site for lipid transport and
97 processing, reminiscent of human hepatocytes. However, whether and how oenocytes
98 regulate tumor growth is unknown.

99 The *Drosophila* trachea is a network of oxygen transporting tubes, the functional
100 equivalent of mammalian blood vessels [40]. Trachea is composed of terminal tracheal
101 cells (TTCs), which are highly plastic cells, and the terminal branches (TBs) or tracheoles
102 which deliver oxygen to the tissues. TTCs are oxygen sensing cells, and hypoxic conditions
103 promote the formation of TBs through hypoxia-inducible factor-1$\alpha$ (HIF-1$\alpha$; Similar (Sima)
104 in *Drosophila*), similar to the role of HIF-1$\alpha$ in mammalian angiogenesis. Trachea resides in
105 proximity of many tissues, including the midgut. Trachea penetrate the visceral muscles to
106 access the intestinal epithelium to supply it with oxygen [41]. The intestinal epithelium is
107 apicobasally polarized, composed of ISCs and their progeny. Damage induced by enteric
108 infection, oxidative agents and tumor growth can increase tracheogenesis on the midgut,
109 which is necessary for efficient damage-induced ISC-mediated regeneration [42, 43].
110 Additionally, tumor-induced tracheogenesis in *Drosophila* is reminiscent of cancer-
111 induced angiogenesis in mammals [42].

112 Using a Drosophila gut tumor model, we uncover a novel mechanism through which
113 gut tumors reprogram lipid metabolism in distal oenocytes to promote both tracheal
114 development and tumor growth. We find that tumors secrete a PDGF/VEGF-like factor,
115 Pvf1, which activates the TORC1-Hnf4 signaling pathway in oenocytes. This activation
116 boosts the production of specific lipids, including very long-chain fatty acids and wax
117 esters, essential for tracheal growth around the tumor. Notably, reducing the activity of
118 Hnf4 and mElo, an elongase involved in generating very long-chain fatty acids, in oenocytes
119 suppress tumor growth, tracheal development, and cachexia-like phenotypes, while also
120 extending lifespan. Additionally, we demonstrate that this regulatory pathway is conserved
121 in mammals, as VEGF-A stimulates lipid metabolism gene expression in human
122 hepatocytes, and tumor-bearing mice exhibit increased hepatic expression of lipid

123 elongation genes. Our findings highlight a previously unrecognized tumor-host interaction,
124 where tumors non-autonomously reprogram distal lipid metabolism to facilitate their
125 growth.

126 **Results**

127 ***Oenocyte lipid metabolism regulated by Hnf4 controls tumor proliferation***

128 To investigate how tumor growth rewires lipid metabolism of the whole fly, we
129 expressed an active form of *Yorkie ( yki$^{3SA}$),* in adult gut stem cells, using the intestinal stem
130 cells (ISCs)/enteroblast driver (*Esg-Gal4* or *Esg-LexA*), hereafter referred to as Yki flies [21].
131 *Esg-Gal4* or *Esg-LexA* was combined with the *tubulin* promoter-driven temperature-
132 sensitive *GAL80 (tubP-GAL80$^{TS}$)* to control the temporal expression of Gal4 or LexA. Next,
133 we conducted untargeted lipidomic profiling using an LC-MS/MS-based platform of whole-
134 body samples of adult female flies (*Esg-LexA* > *LexAop-yki$^{3SA}$*) expressing *yki$^{3SA}$* for 3 days,
135 together with control flies (*Esg* > +). The complete *Drosophila* genotype information can be
136 found in Supplementary Table 1. Female flies are used in the analysis unless otherwise
137 noted because they show more significant and consistent tumor-associated cachexia
138 phenotypes. We detected 2471 lipid species in total representing 45 lipid classes
139 (Supplementary Table 2). The lipidomic analysis showed an increase in wax ester (WE),
140 monogalactosyldiacylglycerol (MGDG), phosphatidylglycerol (PG), phosphatidylcholine
141 (PC), ceramide (Cer) and acylcarnitine (AcCa) levels in Yki flies (Figure 1A). We also
142 observed a slight reduction of triglycerides (TG) in Yki flies at early stage, in agreement with
143 previous findings [21, 44]. WEs are major components of cuticular lipids, which cover
144 nearly all parts of terrestrial arthropods [45] to restrict water loss, and WE levels are
145 significantly increased in Yki flies (Figure 1B), yet the significance of this regulation is
146 unknown. By profiling the fatty acid carbon chain length of WEs, we found that Yki flies
147 exhibit elevated levels of WEs containing very-long-chain fatty acids (carbon length ≥22),
148 as well as WEs with shorter chains (<22) (Figure 1C). As the biosynthesis of cuticular lipids
149 mainly occurs in *Drosophila* oenocytes and Hnf4 is a main regulator of this process [39],
150 we tested whether oenocyte Hnf4 regulates the level of WEs in control flies. WEs were
151 slightly reduced when *Hnf4* was knocked down in control adult oenocytes using the

152 *PromE(800)-Gal4* temperature sensitive driver (*PromE-GAL4,Tub-GAL80*$^{TS}$, referred to as
153 *PromE*). PromE(800)-Gal4 is specifically expressed in adult female oenocytes, although it is
154 also expressed in the reproductive organs of adult males [31]. To ensure tissue specificity,
155 female flies were used in all experiments unless otherwise noted. Next, to test whether
156 Hnf4 regulates WE synthesis in Yki flies, we used the LexA-LexAop system to induce Yki
157 tumors in the gut and the Gal4/UAS system in oenocytes (*PromE-GAL4, Tub-GAL80*$^{TS}$,
158 referred to as *PromE*) to knockdown *Hnf4*. Knockdown of *Hnf4* in oenocytes decreased Yki-
159 induced WE levels (Figure 1D), indicating that *Hnf4* expression in oenocytes is required for
160 the increase of WE.

161 As a nuclear receptor, the localization of Hnf4 is highly enriched in oenocyte nuclei
162 compared to the fat body [39, 46]. To visualize the localization of Hnf4, we tagged the
163 endogenous *Hnf4* gene with 127D01, a small epitope tag that can be detected with a
164 specific nanobody [47, 48], using an homology directed repair pathway CRISPR-Cas9
165 targeted insertion method [47]. To validate the Hnf4-127D01 line, we knocked down *Hnf4* in
166 oenocytes, which significantly reduced its nuclear localization (Figure S1A). Hnf4-127D01
167 in control oenocytes showed high level of nuclear localization, consistent with previous
168 findings (Figure 1E) [46]. Interestingly, increased nuclear localization of Hnf4-127D01 was
169 observed in the oenocytes of Yki flies (Figure 1E-1F). Altogether, these data suggest that
170 oenocytes in Yki flies have increased Hnf4 activity. To test whether oenocyte Hnf4 signaling
171 is required for tumor growth, we measured ISC-mitosis using phospho-histone 3 (pH3+)
172 staining. Downregulation of *Hnf4* in oenocytes of Yki flies *(Esg-LexA>yki*$^{3SA}$-GFP*;*
173 *PromE>Hnf4-i)* for 3 days showed a decrease in pH3+ staining compared to controls (*Esg>*
174 *UAS-yki*$^{3SA}$-GFP), and a slower growth rate for tumor (Figure 1G). Importantly, *Hnf4*
175 knockdown in wild-type animals did not alter pH3+ cell numbers relative to controls (Figure
176 1G), indicating that the requirement for Hnf4 in Yki-driven tumors reflects its tumor-
177 associated mis-regulation rather than a general role in proliferation. To quantify tumor
178 burden, we measured the percentage of GFP-positive area in the gut and found that
179 oenocyte-specific depletion of *Hnf4* in Yki flies markedly reduced GFP-positive area,
180 consistent with tumor regression (Figure S1B-C). We next assessed tumor-induced

181 cachexia phenotypes, including ovary wasting and abdominal bloating caused by fluid
182 accumulation (Figure S1D). Short-term oenocyte *Hnf4* knockdown (3 days) alleviated ovary
183 wasting (Figure S1E), reduced bloating (Figure 1H) and decreased whole-body wet weight
184 (Figure S1F), supporting a role for aberrant oenocyte Hnf4 activity in promoting tumor
185 growth and associated cachexia.

186 Our results suggest that Hnf4 transcriptional activity is induced in oenocytes of Yki
187 flies. To validate this, we measured whether the expression of Hnf4 targets in Yki oenocytes
188 also increased. Hnf4 target genes are involved in beta-oxidation and very long chain fatty
189 acid (VLCFA) biosynthesis in oenocytes [39, 49]. Thus, we tested whether VLCFA
190 biosynthesis genes (*Hnf4, mElo, CG30008, CG16904, FarO, ACC, HDAC, TER, Cyp4g1,*
191 *Cpr*), as well as genes involved in beta-oxidation (*Whd, Scu, Yip2* and *CG7461)* were
192 dysregulated in Yki flies. *CG30008, CG16904, FarO, ACC, HDAC, TER, Cyp4g1, Cpr, Whd,*
193 *Scu, Yip2* showed no difference between control and Yki flies (Figure S1G). However, we
194 observed a significant increase in *mElo* (Figure 1I), which encodes a methyl-branched
195 cuticular hydrocarbon elongase [37], and a minor increase for *Hnf4 and CG7461* (Figure
196 S1G).

197 *mElo* has recently been shown to produce long chain methyl-branched cuticular
198 hydrocarbons in oenocytes that help prevent desiccation [37], a key function of Hnf4 in
199 oenocytes [39]. Additionally, *mElo* expression is highly enriched in control adult oenocytes
200 according to snRNAseq data (Figure 1J). Inhibition of *Hnf4* reduced *mElo* expression, and
201 overexpression of *Hnf4* led to increased levels of *mElo* (Figure S1H-I), consistent with a
202 previous report that *mElo* is a transcriptional target of Hnf4 [39]. Further, *mElo* is highly
203 induced in the oenocytes of Yki flies and this induction is blocked when *Hnf4* is knocked
204 down (Figure 1I).

205 In control flies, reduction of *mElo* in oenocytes did not affect pH3+ number in the
206 gut (Figure 1K). To test the function of oenocyte *mElo* during tumor growth, we reduced the
207 level of oenocyte *mElo* in Yki flies and observed fewer pH3+ in the gut, suggesting that *mElo*
208 contributes to Yki tumor growth (Figure 1K). Similarly, we observed a reduced tumor burden
209 with *mElo* knockdown in Yki flies (Figure S1J). We validated the effectiveness of *mElo*

210 knockdown in the oenocytes (Figure S1K). Unlike *Hnf4,* reducing *mElo* expression in control
211 oenocytes using the gene-switch driver (hereafter referred to as PromE$^{gs}$) [30], where the
212 driver is activated upon mifepristone feeding (RU), did not cause steatosis and affect ovary
213 size, suggesting that other targets of Hnf4 regulate oenocytes steatosis and ovary size
214 (Figure S1L and Figure S1M). Consistently, *mElo* knockdown did not rescue ovary wasting
215 in Yki flies (Figure S1N).
216 To assess whether oenocyte lipid metabolism affects the viability of Yki flies, we
217 inhibited *Hnf4* in oenocytes and observed a significant lifespan extension (Figure
218 1L).Inhibition of mElo in oenocytes of Yki flies also significantly increased lifespan (Figure
219 1M). Finally, *mElo* has a sex specific function in regulating different types of hydrocarbons
220 [37]. Therefore, we tested whether *mElo* also regulates Yki viability in male flies. Strikingly,
221 inhibition of *mElo* also significantly increased the lifespan in Yki males (Figure S1O).
222
223 ***Oenocyte Hnf4 activity is regulated by TORC1***
224 We next sought to determine the factors regulating Hnf4 level in oenocytes. Previous
225 studies have shown that inhibiting the TORC1 pathway in oenocytes leads to steatosis [50],
226 a phenotype that mimics reduced *Hnf4* expression in these cells [39], suggesting that the
227 TORC1 pathway positively regulates *Hnf4* transcription in oenocytes. The Tuberous
228 Sclerosis Complex (TSC) is known to negatively regulate TORC1 by inhibiting RAS homolog
229 enriched in brain (Rheb) activity [51]. Next, we also tested the effects of oenocyte *TSC1,2* in
230 tumor growth. Consistent with *Hnf4* and *mElo* knockdown, *TSC1,2* overexpression in
231 oenocytes reduced tumor induced WE levels (Figure 2A). We also observed an increased
232 level of TORC1 activity, as measured by phospho-4EBP (p4EBP) staining in oenocytes of Yki
233 flies (Figure 2B-C). Additionally, overexpressing *TSC1,2* blocked *mElo* expression in
234 oenocytes of Yki flies (Figure 2D), Yki-induced pH3$^{+}$ cells in the gut (Figure 2E), as well as
235 Yki-induced ovary wasting and bloating (Figure S2A and S2B). Together, these data identify
236 oenocyte TORC1 activation as a key driver of tumor growth and implicate Hnf4 as a
237 downstream effector.

238 To test whether TORC1 regulates *Hnf4* expression level, we analyzed a previously
239 published snRNAseq dataset [50]. Overexpression of *Tsc1* together with *Tsc2* (*TSC1*,2) in
240 oenocytes, which inhibits *TORC1*, resulted in reduced *Hnf4* expression specifically in
241 oenocytes (Figure 2F), but not in muscle nor fat body tissues, suggesting that TORC1
242 positively regulates Hnf4 levels in oenocytes. Next, we examined the protein level of
243 endogenously tagged Hnf4-127D01 following *TSC1,2* over-expression and observed a
244 significant reduction in Hnf4-127D01 levels in oenocytes, particularly in the nucleus as
245 Hnf4 is a transcription factor (Figure 2G-H). Given that Hnf4 regulates hydrocarbon
246 synthesis in oenocytes and its knockdown increases the susceptibility to dry starvation
247 [39], we overexpressed *TSC1,2* in oenocytes and found that it led to an increased sensitivity
248 of flies to dry starvation (Figure S2C). Additionally, as Hnf4 regulates the expression of
249 genes involved in very-long-chain fatty acid (VLCFA) synthesis [39], we analyzed the
250 expression of VLCFA synthesis genes in snRNAseq data from control (*PromE>EGFP*) versus
251 TSC1,2-overexpressing oenocytes (*PromE>TSC1,2*). Using uniform Manifold Approximation
252 and Projection (UMAP), which identifies cell types in mixed populations based on
253 snRNAseq data, we found that VLCFA synthesis genes were highly enriched in oenocytes
254 (Figure 2I). The ModuleScore, calculated by averaging the expression of the VLCFA
255 synthesis pathway genes and subtracting the expression of a randomly selected gene set
256 expression, decreased in oenocytes upon *TSC1,2* overexpression (Figure 2I).
257 Inhibition of TORC1 through overexpressing *TSC1,2,* or overexpressing Proline-rich
258 Akt substrate 40 kDa (*PRAS40)*, or by feeding flies with rapamycin, all induced steatosis in
259 oenocytes (Figure 2J and S2D-E), as observed following *Hnf4* knockdown in oenocytes
260 (Figure S1L). However, simultaneous overexpression of *Hnf4* with *TSC1*,2 prevented the
261 development of steatosis (Figure 2J), indicating that TORC1 regulates oenocyte lipid
262 metabolism via Hnf4. Lastly, *TSC1,2* overexpression also reduced the expression of *mElo*
263 and *FASN2,* which are Hnf4 target genes, and overexpressing *Hnf4* simultaneously blocked
264 this decrease (Figure 2K-L). Together, these findings suggest that Hnf4 acts downstream of
265 TORC1 to regulate lipid metabolism in oenocytes.
266

267 ***ISCs secreted Pvf1 regulates Hnf4 through PvR signaling in oenocytes and affects***
268 ***tumor associated phenotypes***
269 TORC1 activity is regulated through various pathways, one of which includes
270 PDGF/VEGF signaling. Studies have shown that PvR activation can stimulate the TOR
271 pathway [50, 52, 53]. Consistent with this, muscle-secreted Pvf1 can regulate TORC1
272 activity in oenocytes, suggesting that the activation of the TORC1-Hnf4 axis in oenocytes of
273 Yki flies may occur through PvR activation. Yki-expressing ISCs can secrete higher levels of
274 the Pvf1 ligand, which activates PvR signaling in surrounding tissues (Figure S3A) [22].
275 However, *Pvf1* is expressed at low levels in oenocytes and is not significantly induced in
276 oenocytes and muscles of Yki flies (Figure S3A-B). To determine whether tumor secreted
277 Pvf1 non-autonomously activates Hnf4 level in oenocytes, we knocked down *Pvf1*
278 expression in the ISCs of Yki flies (*Esg>yki$^{3SA}$; Pvf1-i*) and observed its effect on Hnf4 nuclear
279 level in oenocytes. *Esg>yki$^{3SA}$; Pvf1-i* significantly reduced the level of Hnf4 nuclear
280 localization compared to *Yki* flies (*Esg>yki$^{3SA}$; Luc-i)* (Figure 3A-B). Consistently, *mElo*
281 expression was reduced in *Esg>yki$^{3SA}$; Pvf1-i* flies compared to Yki flies (Figure 3C). We also
282 tested whether *Pvf1* reduction in Yki flies affects tumor development, like *Hnf4* inhibition in
283 oenocytes. As reported previously [22], inhibition of *Pvf1* in the tumor gut rescues both
284 bloating and ovary wasting (Figure 3D and Figure S3C). Gut tumors in *Esg>yki$^{3SA}$;Pvf1-i* flies
285 exhibited slower growth at early stage, as shown by reduced number of pH3+ cells and less
286 GFP positive area (Figure 3E and Figure S3D).
287 To demonstrate that Pvf1 secreted from Yki tumors directly controls *mElo*
288 expression through PvR, we used the dual Gal4 and LexA systems to reduce *PvR* level in
289 oenocytes while inducing Yki in ISCs. *Esg-LexA>yki$^{3SA}$;PromE>PvR-i* animals showed
290 reduced *mElo* expression (Figure 3F), decreased the level of bloating (Figure 3G) and ovary
291 wasting (Figure S3E), reduced the number of pH3+ cells in gut tumors (Figure 3H) and
292 reduced tumor burden (Figure S3F), and extended lifespan compared to Yki flies (Figure 3I).
293 Altogether, these data suggest that PDGF/VEGF induced by Yki tumor non-autonomously
294 increases Hnf4 activity in oenocytes through PvR.

295 To test whether ISC secreted Pvf1 can induce oenocyte Hnf4 levels under normal
296 physiology, we overexpressed *Pvf1* specifically in adult ISCs (*Esg>Pvf1*) and measured Hnf4
297 nuclear level in oenocytes. *Pvf1* overexpression in ISCs increased nuclear Hnf4 levels
298 (Figure 3J-K), suggesting an increased transcriptional activity as measured by increased
299 level of *mElo* expression (Figure 3L). To test whether ISC-derived Pvf1 activates PvR in
300 oenocytes, we overexpressed an active form of PvR in oenocytes which was associated
301 with increased nuclear Hnf4 level, as well as increased level of *mElo* expression (Figure
302 3O).
303
304 ***Circulating lipids target trachea but not ISCs to promote trachea growth***
305 To identify the lipid species induced by oenocytes in Yki flies, we performed
306 lipidomic analysis on the fly hemolymph of control flies, *Esg-LexA> yki*$^{3SA}$ and *Esg-LexA>*
307 *yki*$^{3SA}$*; PromE>Hnf4-i* flies (Figure 4A, Supplementary Table 3). Among the lipid species that
308 are induced by Yki and decreased by *Esg-LexA > yki*$^{3SA}$*; PromE>Hnf4-i*, the majority are
309 phospholipids including phosphotidyl choline (PC), phosphatidylglycerol (PG) and
310 phosphatidylethanolamine (PE), triglycerides (TGs) and acylcarnitines (AcCa). More
311 specifically, AcCa 24:1 and AcCa 24:2, which are very-long-chain acylcarnitines (C≥22)
312 secreted by mitochondria when metabolism is inhibited, were elevated in Yki flies while
313 reduced by *Hnf4* knockdown (Figure 4B-C). Circulating PC 36:4, and PE 32:5 phospholipids
314 and TG(18:3_16:0_16:1), TG(18:2_16:0_18:0) triglycerides were induced in Yki flies and
315 rescued by *Hnf4* knockdown (Figure 4D-G). Interestingly, PC 36:4 is elevated in the serum
316 and plasma samples from breast cancer patients and TG(18:2_16:0_18:0) is induced in
317 bladder cancer patients [54].
318 PC and PE are major membrane phospholipids and contribute to lipoprotein
319 assembly and lipid transport. Thus, elevated PC/PE could promote tracheogenesis by
320 supporting both membrane biogenesis and lipid delivery needed for tracheal membrane
321 expansion. Increased AcCas and WEs could contribute to tracheogenesis by supporting
322 local energetic demand or increasing the production of reactive oxygen species (ROS). For
323 example, hepatocyte-derived circulating AcCas are required for systemic thermogenesis

324 during cold exposure in mice; in this setting, peripheral tissues—including brown adipose
325 tissue, skeletal muscle, and heart—take up plasma acylcarnitines and oxidize them to
326 support energy metabolism [55]. In insects, lipid transport in circulation primarily relies on
327 lipophorins (Lpps), which are the major lipoproteins. It is produced predominantly by the
328 fat body and delivers neutral lipids to peripheral tissues via the lipophorin receptors
329 LpR1/LpR2, which mediate lipoprotein binding and internalization through endocytic
330 pathways [56, 57]. The increased circulation of PC 36:4 and PE 32:5 in Yki flies suggests an
331 increase in lipoproteins that transport lipids from oenocytes towards trachea or the midgut.
332 The transport of lipids, such as phospholipids, from oenocytes to the trachea or
333 ISCs to promote tumor growth has not been reported [42]. To test whether changes in
334 oenocyte metabolism regulates ISCs growth, we inhibited Hnf4 activity in oenocytes by
335 overexpressing *TSC1,2*, knocking down or overexpressing *Hnf4*, and observed no significant
336 effect on the number of pH3+ cells in the midgut (Figure S4A). This suggests that changes
337 in oenocyte lipid metabolism does not promote ISC proliferation under normal condition.
338 Since 95% of the hemolymph lipids are transported through lipophorin (Lpp) in flies [56],
339 and that low-density lipoprotein (LDL) receptor homologues LpR1 and LpR2 promote Lpp
340 uptake [58], we reduced LpR1 or LpR2 level in the ISCs. However, this had no impact on the
341 trachea area, skeleton length, and only a minor increase in the number of branches in the
342 *LpR1* knockdown condition (Figure S4C-D). Reducing LpR1 and LpR2 activities in the ISCs
343 also did not affect the proliferation (Figure S4E). To validate RNAi knockdown efficiency, we
344 quantified *LpR1* expression in thoraces from flies expressing *LpR1* RNAi under the muscle-
345 specific *Mhc-Gal4* driver (Myosin heavy chain), and *LpR2* expression in fat bodies from flies
346 expressing *LpR2* RNAi under the fat body–specific *Lpp-Gal4* driver (Apolipophorin). Both
347 RNAi lines efficiently reduced their respective target transcripts (Figure S4F-G ). To further
348 examine the role of LpR1 or LpR2 in ISC tumors, we reduced LpR1 and LpR2 levels while
349 overexpressing Yki (*Esg> yki$^{3SA}$;LpR1-i and Esg> yki$^{3SA}$;LpR2-i*), and found that these
350 manipulations did not impair Yki-induced tracheal growth (Figure 4H-J) or prevent Yki-
351 induced ISC proliferation (Figure 4K). These results suggest that ISC proliferation does not

352 rely on circulating lipids in the hemolymph and that circulating lipids control
353 tracheaogenesis instead.
354 We further tested whether disrupting *LpR1* and *LpR2* activities in the trachea could
355 affect tumor growth. It has been reported that restricting tracheal growth delays tumor
356 development [42]. Consistently, knocking down *LpR2*, but not *LpR1*, using a temperature
357 sensitive trachea-specific driver (*btl-GAL4, UAS-srcGFP, Tub-GAL80$^{TS}$,* referred to as *Btl*) in
358 Yki flies prevented Yki-induced ISC proliferation (Figure 4L) and the tumor burden (Figure
359 4M). Consistently, it also reduced the level of bloating (Figure 4N), tracheal number of
360 branches, tube area and skeleton length compared to control flies (*Btl*>+) (Figure 4O-Q).
361 Knocking down *LpR2* in the normal condition also reduced tracheal branch number
362 skeleton length and total tube area (Figure 4O-Q). Reducing *LpR1* and *LpR2* function in the
363 trachea did not alter ISC proliferation under basal conditions (Figure S4F).
364 Interestingly, oenocyte-specific depletion of *LpR2* also altered gut tracheal
365 morphology under basal conditions (Figure S4H-J), reflecting that the trafficking of
366 phospholipids, WEs and AcCas from oenocytes relies on the uptake of LPPs. Altogether,
367 these findings are consistent with a model in which tracheal morphology, rather than ISC
368 proliferation, depends on lipids generated or processed in oenocytes and delivered via
369 circulating LPP particles.
370
371 ***Hnf4-mElo axis in oenocytes mediates lipid metabolism and tracheogenesis***
372 ***induced by Yki tumors***
373 Tumor growth in the adult *Drosophila* midgut has been previously shown to promote
374 tracheole density [42]. Similarly, we observed an increase in the number of trachea
375 branches, total tube area, and total tube length in the surrounding tissue of the Yki midgut
376 (Figure S5A-D). This led us to investigate whether oenocyte lipid metabolism mediated by
377 Hnf4-mElo axis is crucial for trachea growth in the Yki midgut.
378 To explore whether perturbations of lipid metabolism in oenocytes could block Yki-
379 induced tracheogenesis in the midgut, we manipulated lipid metabolism by overexpressing
380 *TSC1,2* or knocking down *Hnf4* or *mElo*. Using the LexA/LexAop and Gal4/UAS systems,

381 overexpressing *TSC1,2* or reducing *mElo* significantly decreased the number of tracheal
382 branches, total tube area, and total tube length in the Yki midgut. Reducing *Hnf4* levels, on
383 the other hand, only decreased the total tube area (Figure 5A-C).
384 In addition, to verify whether midgut secreted Pvf1 regulates tracheal growth, we
385 knocked down *Pvf1* in ISC in addition to Yki overexpression. Reduction of *Pvf1* blocked Yki
386 induced number of branches, tube area and skeleton length (Figure 5D-F), indicating that
387 oenocyte lipid metabolism is important for tracheal growth induced by Yki.
388
389 ***Oenocyte Hnf4 and mElo regulate tracheogenesis in the midgut***
390 Next, we aimed to understand whether oenocyte lipid metabolism controls trachea
391 growth in control guts. Consistent with *Hnf4* knockdown, oenocyte-specific *mElo* reduction
392 and *TSC1,2* overexpression showed reduced level of whole body WE in non-Yki flies (Figure
393 6A-B). WEs are essential parts of the outer layer of the trachea [59-62], and *waterproof*
394 (*wat*), which is involved in biosynthesis of wax, has been implicated in hydrophobic
395 tracheal coating in *Drosophila* embryos [62]. Knocking down *Hnf4* did not affect the
396 transepithelial barrier mediated by septate junctions in the midgut trachea on the midgut,
397 as revealed by red dextran injection experiment (Figure 6C). However, reduction of
398 oenocyte *Hnf4* altered the morphology of trachea associated with the midgut (R2-R4
399 regions) (Figure 6D). Specifically, we observed a reduction in the number of branches and
400 total skeleton length, normalized to the area of the gut surface (Figure 6E-G). Consistently,
401 we also observed a reduction in branch numbers, tube area and skeleton length when
402 *mElo* was knocked down in oenocytes of control flies (Figure 6H-J). The effect of oenocyte
403 Hnf4 on trachea number is not specific to the midgut, as we also observed a reduction of
404 trachea total tube area in the ovary of control flies (Figure S6A-D). We also examined
405 whether Hnf4 and mElo in the fat body contribute to tracheal growth, since the fat body is a
406 major metabolic organ involved in lipid homeostasis and, like oenocytes, shares
407 hepatocyte-like functions in flies [63, 64]. However, knockdown of *Hnf4* and *mElo* using the
408 fat body– and gut-specific GeneSwitch driver *S106-Gal4* [65] did not affect tracheal growth
409 (Figure S6E-J ), in contrast to the marked reduction observed upon oenocyte-specific

410 knockdown. It suggests that oenocytes play a more prominent role than the fat body in
411 regulating tracheal growth. Overexpressing *Hnf4* or *mElo* is sufficient to induce total
412 tracheal tube area and skeleton length in the midguts of control flies (Figure 6K-P). Finally,
413 to eliminate the effect of RU feeding on trachea morphology, we fed control (*PromE>ctrl*)
414 flies and observed no difference in trachea morphology (Figure S6K-M).
415
416 ***VEGF-A reprograms lipid metabolism in hepatoma cells, while hepatic lipid***
417 ***metabolism is altered in tumor-bearing mice***
418 Using the *Drosophila* Yki tumor model, we found that the tumor secreted
419 PDGF/VEGF-like factor Pvf1 can non-autonomously regulate Hnf4 activity in hepatocyte-
420 like cells to promote the production of VLCFA or related lipids. To test whether this
421 mechanism is conserved in mammals, we incubated HepG2 cells with vascular
422 endothelial growth factor A (VEGF-A), which is orthologous to Pvf1 in flies and a potent pro-
423 angiogenic growth factor expressed in many types of tumors. We measured the expression
424 level of ELOVL fatty acid elongase 1 – 7 (*ELOVL1-7*). Incubating HepG2 with VEGF-A for 24
425 hours can significantly increase the level of *ELOVL1, 2, 4, 6* and *7*, suggesting a conserved
426 regulation of PDGF/VEGF on lipid metabolism in hepatocytes (Figure 7A-E). HNF4$\alpha$ plays
427 an important role in hepatocyte lipid metabolism. Consistent with this, *APOB*, an early
428 transcriptional target of HNF4$\alpha$ [66, 67], showed increased expression in HepG2 cells
429 following VEGF-A treatment (Figure 7F), suggesting an increased HNF4$\alpha$ activity.
430 Consistently, we observed an increased level of HNF4$\alpha$ localization in HepG2 cells treated
431 with VEGF-A (Figure S7A-B). We performed lipidomic profiling of conditioned medium
432 collected from HepG2 cultures following VEGF-A treatment and observed a robust
433 increase in WE (Figure 7G), as seen in Yki flies (Figure 1A-C). Together, these results suggest
434 a conserved VEGF-A–driven regulatory mechanism in hepatic lipid metabolism mediated
435 by HNF4α.
436 In addition, we collected liver samples from *KrasG12D/+;Lkb1f/f* (KL) mice, in which
437 tumors were specifically induced in the lungs, and analyzed the expression levels of *Hnf4$\alpha$*,
438 *Elovl1-7* and HNF4$\alpha$ target genes *acetyl-Coenzyme A carboxylase alpha* (*Acaca*), *fatty acid*

439 *synthase* (*Fasn*) in the liver [68-70]. *Hnf4α, Elovl7, Acc1* and *Fasn* showed higher expression
440 level in the tumor bearing mice, compared to control, suggesting that tumor growth in the
441 lung increased HNA4$\alpha$ activity and induced genes involved in lipid metabolism in liver
442 tissues in the KL mouse model (Figure 7H-L). Consistent with the expression data,
443 lipidomic profiling of serum samples with tumor bearing mice and control mice revealed
444 higher level of WE in the tumor mice serum (Figure 7M), which are mostly comprised of very
445 long chain fatty acids (Figure S7C). The lipidomic analysis also showed that out of 147
446 significantly changed lipid species, most of them (118) are induced and only 29 are
447 reduced (Figure S7C). From the summed lipid species, we found that although
448 phosphatidylcholine (PC) and triglycerides (TG) are reduced in tumor bearing mice serum,
449 the majority of other lipid species, such as Acylcarnitine (AcCa), lysophosphatidylcholine
450 (LPC) are highly induced in tumor bearing mice (Figure 7N). Altogether, these data suggest
451 a conserved mechanism of lipid metabolism regulation in hepatocytes by a PDGF/VEGF-
452 like factor and Hnf4 (Figure 7O).
453
454 **Discussion**
455 We reveal a novel mechanism by which gut tumors in *Drosophila* reprogram lipid
456 metabolism in oenocytes to promote tracheal development and tumor growth. Our
457 findings demonstrate that tumors secrete a PDGF/VEGF-like factor, Pvf1, which activates
458 TORC1 activity, triggering the expression of *mElo* through Hnf4 in oenocytes. This TORC1-
459 Hnf4 signaling pathway enhances the production of specific lipids, such VLCFAs and wax
460 esters (WEs), which stimulate tracheal growth, a crucial process for tumor expansion. We
461 also show that reducing Hnf4 or mElo activity in oenocytes suppresses tumor growth,
462 tracheogenesis, and tumor-induced cachexia, while extending lifespan. Additionally, we
463 highlight the conservation of this regulatory pathway in mammals, where VEGF-A
464 stimulates lipid metabolism gene expression in human hepatocytes. Furthermore, lung
465 tumor-bearing mice exhibit increased *Hnf4α* and *Elovl7* expression in peripheral
466 hepatocytes.

467 Pvf1, a tumor-secreted factor, has previously been linked to tumor-induced muscle
468 and fat body wasting, as well as renal dysfunction in *Drosophila* [22, 71, 72]. In this study,
469 we uncover a novel role for tumor-secreted Pvf1 in modulating oenocyte lipid metabolism
470 through TORC1 and Hnf4, which regulates the expression of the oenocyte-enriched gene
471 *mElo* (Figure 3). While Hnf4 activity is known to be induced by starvation and during the
472 developmental transition from pupae to larvae [39, 49], its upstream regulators remain
473 poorly understood. In MEF cells, the HNF4$\alpha$ binding motif is highly enriched in the
474 promoters of TORC1-induced genes [73], suggesting HNF4$\alpha$ mediates the transcriptional
475 activities of TORC1. Here, we demonstrate that TORC1 positively regulates Hnf4 protein
476 levels in the oenocyte nucleus through transcriptional regulation (Figure 2G). However, the
477 precise mechanisms controlling *Hnf4* transcription downstream of TORC1 remain unclear.
478 REPTOR and REPTOR-BP are likely key players in this process, as they are the major
479 effectors of the transcriptional response induced by TORC1 inhibition [74].
480 Previous studies showed that muscle-derived Pvf1 suppresses lipid synthesis in
481 *Drosophila* oenocytes and limits fat accumulation in the fat body through PI3K/Akt/TOR
482 signaling [50]. In contrast, our results indicate that Yki tumor–derived Pvf1 promotes very-
483 long-chain fatty acid synthesis in oenocytes, thereby supporting tumor growth. This
484 difference may reflect tissue-specific effects of Pvf1. Notably, muscle-derived Pvf1 was
485 reported to inhibit oenocyte lipid synthesis, whereas Pvf1 from the fat body and midgut had
486 no detectable effect on oenocyte lipid metabolism or steatosis [50]. What a gut tumor–
487 derived Pvf1 regulates oenocyte lipid metabolism has not been previously examined. One
488 possible explanation is that tissue-specific post-translational modification of Pvf1 alters its
489 activity, as PDGF/VEGF ligands function as disulfide-linked dimers [75, 76]. In addition,
490 Pvf2 and Pvf3 are strongly induced in gut tumors [22], raising the possibility that distinct
491 PVF homo- or heterodimers may generate different downstream signaling outputs [53].
492 Our study identified a novel mode of communication between oenocytes and the
493 gut. Oenocytes produce lipid substrates that support gut tracheal growth, a process crucial
494 for tumor expansion and potentially ISC growth. Like tumors, bacterial infections and
495 epithelial damage also trigger ISC proliferation [77-79], suggesting that oenocyte-secreted

496 lipids may also support stress-induced ISC expansion. Lipids from oenocytes are possibly
497 acquired by the tracheal cells instead of ISCs, as knockdowns of *LpR1* and *LpR2* in ISCs
498 have no effects in tumor growth (Figure 4H-J). In contrast, reducing *LpR2* in tracheal cells
499 was sufficient to decrease tracheal development (Figure 5O-Q). This may be due to the
500 trachea's direct contact with hemolymph, allowing it to actively acquire lipids, while the
501 midgut is covered by visceral muscle and basement membrane [80, 81].
502 The mechanism by which VLCFA metabolism regulates tracheogenesis remains
503 unclear, though it may involve the induction of Reactive Oxygen Species (ROS) in the
504 trachea. ROS has been implicated in the activation of HIF-1$\alpha$/Sima, and VLCFAs is known
505 to induce mitochondrial dysfunction and ROS production [82-84]. Increased ROS levels,
506 through treatments such as paraquat, $H_2O_2$ or bacterial infection, have been shown to
507 induce tracheogenesis in the midgut [42]. Furthermore, manipulating ROS level in the
508 trachea alone can trigger tracheal branching and ISC proliferation [42]. Interestingly,
509 overexpressing *Hnf4* alone in oenocytes could promote tracheogenesis, but does not
510 significantly induce ISC proliferation (Figure S4A). This difference may be attributed to
511 variations in driver strength, with tracheal development occurring prior to ISC proliferation.
512 Our data indicate that wax esters (WEs) and acylcarnitines (AcCas) are elevated in
513 tumor-bearing flies and mice (Figure 1A and 7N). Notably, in both models we observe an
514 increase in WEs containing very-long-chain fatty acids (VLCFAs), consistent with the
515 elevated expression of Hnf4 and fatty acid elongases in the KL mouse liver as well as in
516 oenocytes from Yki flies. Functionally, increased AcCas and WEs could contribute to
517 tracheogenesis by supporting local energetic demand. For example, hepatocyte-derived
518 plasma acylcarnitines have been shown to be required for systemic thermogenesis under
519 cold exposure in mice, where peripheral tissues such as brown adipose tissue, skeletal
520 muscle, and heart take up circulating acylcarnitines and oxidize them to fuel metabolism
521 [55]. In addition, wax esters can serve as high-density neutral lipid reserves that are
522 mobilized to meet energetic demands in diverse physiological contexts (e.g., diapause and
523 reproduction in marine organisms). Alternatively, lipid elevation could promote
524 tracheogenesis by increasing reactive oxygen species (ROS), which has been implicated as

525 a driver of tracheal growth . WEs can be hydrolyzed into fatty acids and fatty alcohols
526 [42, 85]. VLCFAs released from WEs may undergo peroxisomal oxidation, generating $H_2O_2$
527 as a byproduct, which can stimulate tracheogenesis [42]. In parallel, fatty acids can be
528 transported to mitochondria for β-oxidation, and high fatty-acid flux through mitochondrial
529 respiration can increase electron leak from the ETC and elevate ROS production,
530 potentially contributing to tracheogenesis [86]. These studies also leave open the
531 possibility that metabolites derived from these lipid species act as signaling molecules
532 that promote tracheogenesis.
533 Additionally, increased AcCas and WEs could contribute to tracheogenesis by
534 supporting local energetic demand. For example, hepatocyte-derived plasma
535 acylcarnitines have been shown to be required for systemic thermogenesis under cold
536 exposure in mice, where peripheral tissues such as brown adipose tissue, skeletal muscle,
537 and heart take up circulating acylcarnitines and oxidize them to fuel metabolism [55]. In
538 addition, WEs can serve as high-density neutral lipid reserves that are mobilized to meet
539 energetic demands in diverse physiological contexts (e.g., diapause and reproduction in
540 marine organisms). These studies also leave open the possibility that metabolites derived
541 from these lipid species act as signaling molecules that promote tracheagenesis.
542 We observed that VEGF-A stimulates lipid metabolism gene expression in human
543 hepatocytes, and lung tumor-bearing mice showed increased expression of *Hnf4α* and
544 *Elovl7* in peripheral hepatocytes. This work provides new insights into tumor-host
545 interactions, challenging the conventional view that tumor-associated metabolic changes
546 are merely passive processes and instead demonstrating their role in promoting tumor
547 growth. Specifically, inhibiting *Hnf4* and *mElo* in oenocytes slows tumor growth, halts
548 tumor-induced cachexia, and extends the lifespan of flies (Figure 1 and Figure S1). Yki
549 activation increased levels of AcCas, PCs, and TAGs in the hemolymph, and inhibiting *Hnf4*
550 in oenocytes reversed these lipid changes induced by Yki (Figure 4A). This study identifies
551 the TORC1-Hnf4-Elovl7 axis and tumor-induced lipid metabolism as potential therapeutic
552 targets for managing tumor growth or as biomarkers for early tumor detection.

553 Hnf4 is a master regulator of multiple metabolic pathways in *Drosophila* and
554 inhibiting it could have broad effects on the host. For instance, knocking down *Hnf4* in non-
555 tumor-bearing flies led to increased steatosis (Figures S1L). These wide-ranging effects
556 may limit the efficacy of Hnf4 inhibition as an anti-tumor strategy. In contrast, mElo, which
557 is more specifically involved in lipid elongation, presents a more targeted inhibition with
558 lower toxicity and a greater extension of lifespan (Figures 1M, S1O). Our study also
559 suggests a potential role for elongases in tumor-induced angiogenesis, as overexpression
560 of ELOVL7 has been linked to prostate cancer and is required for cancer growth [87]. While
561 mElo is exclusively expressed in oenocytes in flies (Figure 1J), its ortholog, ELOVL7, is
562 widely expressed in multiple tissues, including the prostate, kidney, brain, small intestine,
563 and thyroid [88]. It is plausible that ELOVL7 is upregulated in various tissues in cancer
564 patients, indicating additional tissue targets for anti-angiogenic therapies.
565 The regulation of *mElo* by Hnf4 seems to be prominent and specific compared to
566 other transcriptional targets under normal physiological conditions (Figure 1I and S1G). It
567 further suggests that the tumor-associated metabolic milieu may reshape Hnf4-driven
568 transcription, potentially by altering (i) cofactor interactions and/or (ii) ligand availability,
569 thereby promoting selective activation of downstream targets such as mElo. Supporting
570 this concept, previous studies demonstrate that HNF4$\alpha$ transcriptional output is context-
571 dependent and influenced by partner proteins: for instance, HNF4$\alpha$ can cooperate with
572 ChREBP (carbohydrate response element-binding protein) to stimulate lipogenic gene *Fasn*
573 during feeding [68, 70], whereas under fasting conditions it can interact with *Foxo1* to
574 enhance expression of gluconeogenic genes such as *G6Pase* [89]. Moreover, HNF4$\alpha$
575 activity can be modulated by long-chain fatty acids [46], raising the possibility that changes
576 in lipid availability in tumor-bearing flies (e.g., due to TAG mobilization) may further
577 influence Hnf4 activity and target selection. Collectively, these findings support a model in
578 which tumor-induced shifts in Hnf4 cofactors and/or lipid ligands redirect Hnf4
579 transcriptional program in Yki oenocytes, leading to robust *mElo* induction.
580 In summary, our data reveal a novel paradigm in which growing tumors actively
581 acquire substrates for tracheogenesis by secreting a PDGF/VEGF-like factor that activates

582 the TORC1-Hnf4 axis in distal oenocytes, inducing the expression of mElo. This promotes
583 the synthesis of VLCFAs, which are transported to the trachea to further support tumor
584 growth (Figure 7O).
585
586 **Materials and Methods**
587 ***Drosophila stocks and husbandry***
588 All experiments were conducted using female flies due to their more consistent
589 bloating phenotype and larger oenocyte, which facilitated dissection. For temperature-
590 sensitive experiments, fly crosses were set up and maintained under a 12:12 hour
591 light:dark cycle at 18°C. Crosses were discarded after 5 days to maintain consistent
592 population density. Following eclosion, adult flies were collected and kept at 18°C for 2–3
593 days. GAL80$^{TS}$ driver activation was achieved by incubating the flies at 29°C for the
594 durations specified in each experiment. For experiments involving the GeneSwitch driver,
595 fly crosses were maintained at 25°C under a 12:12 hour light:dark cycle and discarded after
596 3 days. Adult progenies were collected and fed on food containing 200 μM RU486
597 (Mifepristone, Cayman Chemicals, 10006317), prepared by dissolving the compound in
598 95% ethanol before adding it to standard fly food. Flies were fed on RU486-containing food
599 for 7 days. Esg$^{ts}$ (*esg-Gal4, UAS-GFP, tub-GAL80$^{TS}$*), *Esg-LexA* and *LexAop-yki$^{3SA}$-GFP, Attp40*
600 *UAS-Luciferase* are from the Perrimon lab stock collection.
601 The following strains were obtained from the Bloomington *Drosophila* Stock Center
602 (BL), Vienna Drosophila Resource Center (V) and flyORF (F): *UAS-Hnf4 RNAi* (BL# 29375),
603 *UAS-mElo RNAi* (BL# 44510), *UAS-yki$^{3SA}$* (BL#28817), *UAS-Pvf1-3xHA* (F002862), *UAS-*
604 *PvR[A]* (BL#58496), *UAS-Pvf1 RNAi* (V#102699), *UAS-PvR RNAi* (V#43459), *UAS-Luciferase*
605 *RNAi* (BL#31603), Oe$^{ts}$ (*Desat1-Gal4, tubP-Gal80*) (BL# 65406), *UAS-LpR1 RNAi* (BL#
606 50737), *UAS-LpR2 RNAi* (BL# 54461).
607 *UAS-Hnf4* is a gift from Dr. Carl Thummel [46]; *UAS-TSC1, TSC2* is a gift from Dr.
608 Christen K Mirth [90] and UAS-PRAS40 was a gift from Dr. Aurelio Teleman [91], Btl$^{TS}$ (*Btl-*
609 *Gal4, UAS-srcGFP*) and *QF6 >QUAS-mtdTomato* was a kind gift from Dr. Chrysoula Pitsouli
610 [42]. PromE$^{GS}$(*PromE-GeneSwitch-Gal4*) was a gift from Dr. Heinrich Jasper [92]. *UAS-*

611 *CG18609* and *mFas-Gal4* were gifts from Dr. Henry Chung [93, 94]. *UAS-PRAS40* is a gift
612 from Dr. Aurelio A Teleman [74].
613 Hnf4-127D01 was generated through CRISPR-mediated tagging of endogenous Hnf4
614 with 127D01-tag as described previously [47]. Briefly, we cloned the sequence 1 kb
615 upstream and 1 kb downstream of the stop codon into the donor vector pScarlessHD-C-
616 3x127D01-DsRed (Addgene#171578). A sgRNA plasmid pCFD3-Hnf4-sgRNA that target the
617 seed sequence (CCAGAGACTGGTTACTAGAAGAA) near the stop codon of Hnf4 was injected
618 into yw;nos-cas9/CyO embryos together with the donor plasmid. Positive transformants
619 with red eye fluorescent eyes were outcrossed and successful Kis were confirmed by PCR
620 (F: GTACAACCGGAGCGAGGGTA; R: CAAAATGGTTCAAGGCATAACA) and sequencing.
621 Subsequently, 3xP3dsRed was excised using piggyBac transposase (BL#8285).
622
623 ***Untargeted lipidomic analysis***
624 Lipidomics and metabolomics of fly samples was performed following the Folch
625 method (Folch et al., 1957). 15 adult flies, 20ul of mice serum and hemolymph from 200-
626 300 adult flies were used for lipidomics and metabolomics. Solid samples were
627 homogenized in a 1 mL Dounce homogenizer (TIGHT) on ice with 0.6 mL chloroform and 0.3
628 mL methanol (2:1 chloroform-methanol mixture). Homogenized samples were transferred
629 to a 15 mL glass tube with a Teflon cap, and an additional 0.6 mL chloroform and 0.3 mL
630 methanol were added to make the final volume approximately 1.8 mL. Hemolymph
631 samples or conditioned medium was transferred to a 15 mL glass tube containing 2:1
632 chloroform-methanol mixture. Samples were vortexed briefly and incubated at room
633 temperature on a rotator for 30–45 minutes. Following incubation, 0.2 volumes (0.36 mL) of
634 HPLC-grade deionized water (HPLC dH2O) were added. The mixture was vortexed three
635 times, followed by centrifugation at 1000 × g for 10 minutes at 4°.
636 The upper aqueous phase, containing polar metabolites, was carefully collected
637 using a glass pipette, while avoiding the middle phase. Metabolites were transferred to
638 microcentrifuge tubes, evaporated under vacuum using a SpeedVac rotary evaporator
639 overnight, and stored at -80°C. Polar metabolites were resuspended in 20 μL of HPLC-grade

640 water and then injected and analyzed using a hybrid 6500 QTRAP triple quadrupole mass
641 spectrometer (AB/SCIEX) connected to a Prominence UFLC HPLC system (Shimadzu). The
642 lower phase, containing non-polar lipids, was transferred to a clean 1.85 mL glass test tube
643 using a glass pipette. The phase was dried under nitrogen gas for approximately 30
644 minutes, and dried lipids were stored at -80°C to prevent oxidation. Non-polar lipids were
645 resuspended in 35 µL of HPLC-grade 50% methanol/50% isopropyl alcohol (IPA) and then
646 injected and analyzed using untargeted high-resolution LC-MS/MS on a Thermo QExactive
647 Plus Orbitrap mass spectrometer. LipidSearch version 4.2 (Thermo Scientific) was used to
648 identify lipid molecules, with the quantification of ion intensity by measuring the area size
649 of identified peaks.
650 The full names of the lipid species can be found in Supplementary Table 4. For
651 lipidomic quantification using whole fly bodies, the same number of flies was used for lipid
652 extraction. Lipid species were normalized to the total reads in each sample. For
653 hemolymph lipidomic analysis, lipid species were normalized to both the volume of
654 hemolymph extracted and the total reads in each sample.
655
656 ***RNA extraction Quantitative RT-PCR***
657 Adult female fly oenocytes were dissected in cold 1xPBS before RNA extraction. For
658 oenocyte dissection, the fat body was removed through liposuction and then oenocytes
659 were removed from the cuticle using a fine-tip glass needle. Tissue lysis, RNA extraction,
660 and cDNA synthesis were performed using Cells-to-CT Kit (Thermo Scientific, #44-029-53).
661 For female adult whole body mRNA extraction, four flies per biological replicate were
662 collected. Total RNA was extracted using Direct-zol RNA MicroPrep kit (Zymo Research,
663 #R2060). mRNA was extracted from HepG2 cells using Directo-zol RNA MicroPrep kit
664 (Zymo Research, #R2060). 30-50mg of mice livers were dissected and total RNA was
665 extracted using Qiagen RNeasy Mini kit (Qiagen #74104). All the cDNAs were synthesized
666 using the iScript cDNA synthesis kit (Bio-Rad, #1708896) in a 40ul reaction mixture using
667 1000ng total RNA. Quantitative real-time RT-PCR (RT-qPCR) assays were performed using
668 iQ SYBR Green Supermix (Bio-Rad, #1708880) on a CFX96 Real-Time PCR Detection

669 system (Bio-Rad). Two to four independent biological replicates were performed with two
670 technical replicates. The mRNA abundance of each gene was normalized to the expression
671 of *RpL32* or *αTub84B* for fly samples, Gapdh for mouse samples and ACTB for HepG2
672 samples. Primer sequences are listed in the Supplementary Table 5.
673
674 ***Fly imaging***
675 *Drosophila* ovaries were dissected in cold PBS. ovaries were imaged immediately in
676 cold PBS using a ZEISS Axiozoom V16 fluorescence microscope. Flies were anesthetized
677 on $CO_2$ pad and imaged using ZEISS Axiozoom V16 fluorescence microscope. The size of
678 the ovary and abdomen is measured using Fiji (version: 2.14.0/1.54f).
679
680 ***Oil Red O staining***
681 The method was as previously described [29]. Flies were dissected in PBS and fat
682 bodies were removed with liposuction. Specimens were fixed in 4% paraformaldehyde for
683 20 minutes. Specimens were rinsed twice with distilled water. Oil Red O (O0625-, Sigma-
684 Aldrich) was dissolved in isopropanol to make 0.1% Oil Red O stock. A working solution
685 was prepared by combining 3 mL of 0.1% Oil Red O in isopropanol with 2 mL of distilled
686 water. The solution was freshly prepared and filtered through a 0.2-μm syringe filter before
687 use. Specimens were incubated for 25 minutes in Oil Red O stain, rinsed briefly with PBS
688 and mounted in Vector Shield for imaging. Oil Red O images were taken using Olympus
689 VS200 Slide Scanner, equipped with color camera (2448x2048 pixels, 3.45μm).
690
691 ***Immunostaining and image analysis***
692 For immunostaining using the nanobodies, fly abdomens were dissected in PBS at
693 room temperature with fat bodies removed and fixed in 4% formaldehyde in PBS for 30
694 minutes. Specimens were washed three times in PBST (0.1% Triton-X-100), 5 minutes each.
695 The specimens were then incubated in 5% NGS (normal goat serum in PBST) for 1 hour.
696 Nb127D01-ALFA, 0.2mg/ml was used at a dilution of 1:500, incubating the samples for 1
697 hour and a half with mild shaking. Followed by 0.1% PBST washes, 5 minutes each wash.

698 AlexaFluor 594 anti-Alpaca (Jackson Immuno Research, 128-585-232) was diluted 1:400 in
699 PBS-TX + 5% NGS and incubate with the specimens at room temperature with mild shaking
700 for 1 hours. After washes and DAPI staining, tissues were mounted in Vectashield and
701 imaged with Olympus VS200 Slide Scanner or confocal microscope Zeiss Axio Observer Z1.
702 For regular immunostainings, fly tissues were dissected in PBS at room temperature.
703 Tissues were fixed in 4% paraformaldehyde in PBS for 30 minutes. Specimens were washed
704 three times in 0.1% PBST and incubated in 5% NDS solution for 1 hour. Tissues were then
705 incubated with primary antibodies diluted in PBST and blocking solution overnight at 4°.
706 Then the tissues were washed three times with PBST at room temperature. Secondary
707 antibodies were applied for 1 hour. Excess antibodies were washed in PBST, and tissues
708 were incubated with DAPI (Invitrogen, D1306) dilute in PBST for 5 minutes. Tissues were
709 then mounted in Vectashield (Vector Laboratories Inc, H-1000). The following primary
710 antibodies were used: rabbit-anti-pH3 (1:500, Cell Signaling, 9701), rabbit-anti-p4E-BP
711 (1:800, Cell Signaling, 2855S). Secondary antibodies against mouse, rabbit, chicken or
712 alpaca conjugated to Alexa Fluor 488 and 594 (Jackson Immuno Research) were used at
713 1:800 for anti-p-4EBP, 1:1000 for anti-pH3 and 1:400 for Nb127D01-ALFA.For
714 immunostaining in HepG2 cells, cells were washed twice with PBS and fixed in 4%
715 paraformaldehyde for 25 min, followed by a PBS wash. Samples were permeabilized with
716 0.5% Triton X-100 in PBS for 10 min and washed with PBS. Non-specific binding was
717 blocked in 1% BSA in PBS for 1 h at room temperature. Cells were then incubated with anti–
718 HNF4α rabbit monoclonal antibody (C11F12, Cell Signaling Technology, #3113) diluted
719 1:1000 in PBS at 4 °C overnight. After washing twice with 0.05% Triton X-100 in PBS,
720 samples were incubated with Alexa Fluor 594–conjugated secondary antibody (1:500 in
721 PBS) at room temperature. Cells were washed three times with 0.05% Triton X-100 in PBS
722 and once with PBS, then mounted using SlowFade® Gold antifade reagent with DAPI
723 (Invitrogen, S36939) and sealed with a coverslip.
724 Quantification of nucleus Hnf4 intensity was conducted using ImageJ. Background
725 subtraction was performed using the rolling ball radius at 50 pixels. We apply threshold to

726 the DAPI channel and using analyze particles to select nucleus as Region Of Interest (ROI),
727 size: 10-2000; circularity: 0.1-1. Mean gray value was measured for each ROI.
728
729 ***Lifespan analysis***
730 For survival analysis, flies were collected within 24 hours post-eclosion (20 females
731 and 3 males per vial) and maintained on standard laboratory fly food at 18°C, with 60%
732 humidity, and a 12-hour light/dark cycle. After two days, mature and mated females were
733 transferred to 29°C to induce gene expression. To maintain vial cleanliness, flies were
734 transferred to fresh vials every two days, and the number of dead flies was recorded daily.
735
736 ***snRNAseq analysis***
737 Data and plots were generated from the Fly Cell Atlas, generated using the 10X
738 platform, "Stringent All" dataset. Other snRNAseq dataset was analyzed as described in
739 [50], where a resolution of 0.4 was chosen as the clustering parameter.
740 For the Seurat Module Score analysis, Seurat AddModuleScore function was used to
741 calculate the average expression of a group of genes in Very Long Chain Fatty Acid
742 Synthesis pathway in each cell (for details of the list, see Supplementary Table 6), then
743 subtracted by a randomly picked gene set expression.
744
745 ***Rapamycin feeding***
746 Rapamycin was dissolved in DMSO to make 2mM rapamycin stock. Rapamycin
747 stock was further diluted to 200μM in ethanol and evenly distributed on to food surface. A
748 small piece of Kimwipe was used to remove excess liquids on the food. DMSO dissolved in
749 ethanol was used as control. Flies were transferred to new food every two days. Flies were
750 fed for 6-7 days before dissection.
751
752 ***Dextran injection***
753 Using a fine glass needle, ~100nl of 50 mg/ml 10,000 MW TR-dextran (Thermo Fisher
754 Scientific, D-1817) diluted in water was injected in the abdomen of adult females. 6 hours

755 after injection, abdomen and thoraces were separated and whole abdomen were fixed in
756 4% paraformaldehyde for 30 minutes with mild shaking. After fixation, midguts were
757 dissected and washed briefly with PBS and mounted in Vectashield. Midguts were imaged
758 using a single point laser scanning confocal, Olympus IX83 to measure the trachea
759 leakage. A Z-stack was taken, and maximum projections were used to generate final image
760 for analysis.
761
762 ***Trachea imaging***
763 Generating fly strains that incorporate both a trachea reporter and other genetic
764 modifications is challenging. Therefore, the following method, as described in [42], was
765 used to quantify the trachea. Flies were dissected in cold PBS, and intestines were
766 carefully extracted to maintain their original structure. Tissues were then fixed in 4%
767 paraformaldehyde for 20 minutes, mounted in Vectashield, and imaged within 3 days.
768 Whole intestine images were captured using an Olympus VS200 Slide Scanner equipped
769 with a color camera. Only the upper layer of the tissue, in contact with the coverslip, was
770 analyzed.
771
772 ***Trachea analysis***
773 To automate trachea measurement, we used the previously developed software
774 AutoTube [95]. Only the topmost Z-stack, which provided the clearest image of the trachea,
775 was analyzed. Images corresponding to the R2-R4 regions of the gut were cropped,
776 avoiding areas with the major trunk of the trachea to prevent skewing the results. Images
777 were thresholded on a white background and analyzed with AutoTube using the following
778 settings:
779 - Input Color Channel: Green
780 - Intensity adjustment: Autocontrast
781 - Illumination correction: Illumination size set to 51
782 - Noise correction: BM3D
783 - Tube detection: Finer tubes with a tube size of 3

784 - Small regions removed: 0.01% of Ima
785 - Hole filling: Hole size set to 1
786 - Threshold type: MultiOtsu
787 - Short ramifications removed: Spur length set to 15
788 - Spatial branch merging: Spatial distance set to 10
789 The analysis provided results for "Number of Branches (μm)," "Total Tube Area (μm)," and
790 "Total Skeleton Length (μm)," which were normalized to the corresponding intestinal area
791 and were multiplied by an arbitrary number 1000000. Results from the R2-R4 regions were
792 averaged for each gut.
793
794 ***Animal care and tumor induction***
795 *Kras*$^{G12D}$*/+;Lkb1*$^{f/f}$ mice, previously described [7, 96], were backcrossed to the FVB
796 strain. Male mice were maintained on a 12-hour light/dark cycle at an ambient temperature
797 of 22°C, with ad libitum access to rodent chow (PicoLab Rodent 5053; Lab Diet, 3.43
798 kcal/g) and drinking water. Tumors were induced in adult male and female mice (12 to 20
799 weeks old) via intranasal administration of 75 μL PBS containing $2.5 \times 10^7$ pfu of adenovirus
800 SMV-CRE (Ad5CMV-Cre) purchased from the University of Iowa Gene Transfer Vector Core
801 (Iowa City, IA). All animal experiments were conducted with the approval of the Institutional
802 Animal Care and Use Committee (IACUC) at Weill Cornell Medicine (WCM) under protocol
803 number 2013-0116.
804
805 ***Mice tissue collection***
806 Male mice were euthanized with $CO_2$, followed by blood collection via cardiac
807 puncture. Liver, gonadal adipose tissue, and skeletal muscles were dissected and flash-
808 frozen in liquid nitrogen and stored at -80°. The control mice were a mix of fasted and fed
809 mice. “Fasted” mice were fasted for 12 hours and “fed” mice were fasted for 12 hours and
810 then allowed free access to food for 4 hours before tissue collection.
811
812 ***VEGFA incubation***

HepG2 cells were cultured in HyClone Dulbecco's Modified Eagle Medium (DMEM) with high glucose (SH30022.01): with L-glutamine; without sodium pyruvate. Additional 50U penicillin/ml and 50ug streptomycin/ml were added. HepG2 cells were seeded at density of 5 x $10^5$ in 12-well-plate (VWR, 29442-040), treated or not with 50ng/ml Recombinant Human VEGF 165 (PeproTech, 100-20-2UG) for 24 hours. Total cellular RNA was isolated using the Trizol reagent and extracted through Direct-zol RNA MicroPrep kit (Zymo Research, #R2060).

**Acknowledgments**

We thank Dr. John M. Asara at the Beth Israel Deaconess Medical Center for his help on lipidomic analysis. We thank the assistance provided by the Microscopy Resources on the North Quad (MicRoN) core and we thank Dr. Simon F. Norrelykke at the Image Analysis Collaboratory at Harvard Medical School for advice on AutoTube. We also thank Dr. Ah-Ram Kim, Dr. Sun Jin Moon at Harvard Medical School, Dr. Hua Bai at Iowa State University, Dr. Eileen White and Dr. Maria Gomez- Jenkins at Rutgers University for scientific discussion and insights. We thank Dr. Ju Xu at Chinese Academy of Sciences for the help generating Hnf4-127D01 fly strain. We thank Dr. Ying Liu at Harvard Medical School for sharing fly lines used in this study. We also thank Christians Villalta for the help on fly dextran injection.

This article is subject to HHMI's Open Access to Publications policy. HHMI lab heads have previously granted a nonexclusive CC BY 4.0 license to the public and a sublicensable license to HHMI in their research articles. Pursuant to those licenses, the author-accepted manuscript of this article can be made freely available under a CC BY 4.0 license immediately upon publication.

**Funding**

This work is funded by NIH/NCI Grant #5P01CA120964-15 and is delivered as part of the CANCAN team supported by the Cancer Grand Challenges partnership funded by Cancer Research UK (CGCATF-2021/100022) and the National Cancer Institute (1 OT2

842 CA278685-01). This work is funded by the Hypothesis Development Award from DOD
843 CDMRP TSCRP (GRANT14223060). N.P. is an investigator of the Howard Hughes Medical
844 Institute.
845
846 **Author contributions**
847 Conceptualization: KH, TM, MG, NP; Methods, Data Acquisition, Resources,
848 Visualization and Imaging: KH, TM, YC; Mice sample preparation: ED, JS; Data Acquisition:
849 KW, Bioinformatic Analysis: MH, YH, SJM; Independent replication of experiments at
850 Harvard Medical School: KH; Writing – original draft: KH, Writing – review, editing & revising:
851 KH, TM, NP.
852
853 **Figure 1: Oenocyte Hnf4 regulates wax ester synthesis and supports Yki-induced**
854 **tumor growth.**
855 (A-B) Heatmap of the normalized total ion intensity of major lipid classes identified in
856 whole bodies from control flies (*Esg-LexA*) or Yki flies (*Esg-LexA/LexAop-yki*$^{S3A}$*; PromE-*
857 *GAL4, Tub-GAL80*$^{TS}$/+), with four biological replicates per condition. Scaled colors are
858 presented as the values relative to the average of each row. (B) Untargeted lipidomic
859 profiling using LC-MS/MS of whole-body extracts revealed increased wax ester (WE) levels
860 in Yki flies. Normalized intensity was calculated as the integrated LC–MS peak area for
861 each lipid species, normalized to the sample's total signal (total reads) and to the analyzed
862 sample volume. (C) Fatty acid chain-length distribution ($C < 22$ and $C \geq 22$) in detected WE
863 level from control and Yki flies. (D) WE level in control flies, Yki flies, and *Hnf4* knockdown
864 in oenocytes of Yki flies, N = 4 biological replicates. (E-F) Immunostaining of Nb127D01 for
865 nuclear-localized, endogenously tagged Hnf4 (Hnf4-127D01) in oenocytes in controls and
866 in Yki flies. DAPI staining marks nuclei, with dashed lines enclosing oenocytes. N = 8
867 independent experiments. (G) Quantification of intestinal stem cell (ISC) proliferation, as
868 indicated by phospho-histone H3 (pH3+) cells in control. (H) Bloating as measured by
869 abdominal area of the fly in control, oenocyte specific Hnf4-i, Yki flies and Yki flies with
870 oenocyte specific Hnf4-i. (I) *mElo* expression in oenocytes, normalized to housekeeping

871 gene, in control, oenocyte specific Hnf4-I, Yki flies and in Yki flies with *Hnf4* knockdown. N
872 = 2 biological replicates from 2 independent experiments. (J) UMAP from whole body
873 (without head) snRNAseq, *mElo* expression is enriched in adult oenocytes. (K)
874 Quantification of pH3+ cell number, N =8 flies. (L-M) Lifespan analysis showing that
875 oenocyte-specific knockdown of *Hnf4* (L) or *mElo* (M) in Yki flies, compared to only Yki or
876 control flies, N = 40. Scale bar shows 20μm. Data are presented as mean ± s.e.m.
877 Statistical significance was determined using Student's t-test or one-way ANOVA with
878 appropriate post hoc tests, or Log-rank (Mantel-Cox) test. *P < 0.05, **P < 0.01, ****P <
879 0.0001.
880
881 **Figure 1S: Hnf4 and mElo regulate metabolic and tumor-related phenotypes in Yki**
882 **flies.**
883 (A) Immunostaining of Nb127D01 for nuclear-localized, endogenously tagged Hnf4 (Hnf4-
884 127D01) in oenocytes with *Hnf4* knockdown or control flies, with dashed lines enclosing
885 oenocytes. (B-C) Level of GFP positive region in the whole fly midgut in control, oenocyte
886 specific *Hnf4-i* and *Yki* flies with *Hnf4-i*. (D) Abdominal area of control and Yki flies for
887 bloating measurement. (E) Ovary size in control flies, oenocyte specific *Hnf4-i* flies, *Yki* flies
888 and *Yki* flies with oenocyte specific *Hnf4-i*, n = 9 - 15. (F) Wet weight measurement of fly
889 whole body, where flies were weighed first and were dried at 65°C for 5 hours, the second
890 value was subtracted from the first to obtain the wet weight of the fly. N = 3 biological
891 replicates. (G) Expression of VLCFA biosynthesis and β-oxidation genes in control and Yki
892 flies. (H-I) *mElo* expression measured by qPCR in oenocyte specific *Hnf4* knockdown or
893 *Hnf4* overexpression, N = 2 biological replicates from 2 independent experiments. (J) Level
894 of GFP positive region in the whole fly midgut in control, Yki flies, oenocyte specific *Hnf4*-i
895 and *Yki* flies. (K) Confirmation of *mElo* knockdown efficiency via qPCR, N = 2 biological
896 replicates from 2 independent experiments. (L) Oil Red O staining in oenocytes of *Hnf4*
897 knockdown or *mElo* knockdown. N = 8 flies. (M) Ovary size measurement in control and
898 *mElo-i* flies, N = 13-16 flies. (N) Ovary size in control, Yki and Yki with *mElo-i* flies. (O)
899 Lifespan analysis in Yki-expressing flies upon oenocyte-specific *mElo* knockdown in male

900 flies. Data represent mean ± s.e.m.; significance assessed using appropriate statistical
901 tests.
902
903 **Figure 2: TORC1 regulates Hnf4 activity and lipid metabolism in oenocytes.**
904 (A) Whole body WEs level in ISC Yki flies and Yki with oenocyte *TSC1,2* overexpression. (B-
905 C) P-4EBP immunostaining indicates TORC1 activity in oenocytes of Yki flies, quantification
906 of P-4EBP intensity is shown on the right (C), N = 8-10 flies. (D) *mElo* expression in whole
907 body mRNA extracts in Yki flies and Yki flies with *TSC1,2* overexpression in oenocytes, N = 6
908 biological samples. (E) Quantification of pH3+ cell number, N = 8 – 10 flies. (F) Violin plot of
909 *Hnf4* expression in fat body, muscle and oenocytes upon overexpression of *TSC1,2* in
910 oenocytes [12]. (G-H) Immunostaining of Hnf4-127D01 in oenocytes when *TSC1,2* is
911 overexpressed in oenocytes compared to control. DAPI marks nuclei, with dashed lines
912 enclosing oenocytes, quantification of Hnf4-127D01 signal intensity in the nucleus, N = 8-
913 10 flies. (I) ModuleScore from snRNAseq analysis visualizes VLCFA synthesis gene
914 expression across muscle, fat body and oenocytes, in control and upon oenocyte *TSC1,2*
915 overexpression. (J) ORO staining indicates steatosis in oenocytes induced by *TSC1,2*
916 overexpression, and in *TSC1,2* with *Hnf4* overexpression, N = 8. (K-L) Expression of Hnf4
917 targets *mElo* and *FASN2* in *TSC1,2* overexpression and in *TSC1,2* with *Hnf4* overexpression.
918 N = 2 biological replicates from 2 independent experiments.
919
920 **Figure 2S: The role of oenocyte TORC1 in regulating lifespan, steatosis and Yki wasting**
921 **phenotype.**
922 (A-B) Ovary size measurements and bloating are rescued by *TSC1,2* overexpression in Yki
923 flies, N = 15-30 flies. (C) Sensitivity to dry starvation in flies overexpressing *TSC1,2* in
924 oenocytes compared to controls. Adult oenocyte specific driver (*mFas-Gal4*) was used
925 [93]. (D-E) ORO staining indicates steatosis in oenocytes with *PRAS40* overexpression, or in
926 rapamycin treatment. Dashed lines enclose oenocytes in all images. Data represent mean
927 ± s.e.m.; statistical significance determined using Student's t-test or ANOVA as
928 appropriate.

929

930 **Figure 3: ISCs secreted Pvf1 activates Hnf4 through PvR signaling in oenocytes and**
931 **affects tumor associated phenotypes.**
932 (A-B) Hnf4 immunostaining in oenocytes of Yki flies with ISC-specific Pvf1 knockdown.
933 Dashed lines enclose oenocytes. N = 10 biological replicates. (C) *mElo* expression in
934 oenocytes of Yki flies with ISC-specific Pvf1 knockdown, N = 4 biological replicates from 2
935 independent experiments. (D) Inhibition of *Pvf1* in the gut affects bloating in Yki flies, n =
936 15-20 flies. (E) ISC proliferation in Yki flies with *Pvf1* knockdown, n = 8-10 biological
937 replicates. (F) *mElo* expression in oenocytes of Yki flies with *PvR* knockdown. N = 2
938 biological replicates from 2 independent experiments. (G-H) *PvR* knockdown in oenocytes
939 of Yki flies and its effect on tumor-associated bloating (G) and pH3+ cell number (H). (I)
940 Lifespan extension in Yki flies with oenocyte-specific *PvR* knockdown, N = 40 flies. N = 10
941 biological replicates. (J) Hnf4 immunostaining in oenocytes of flies with ISC-specific *Pvf1*
942 overexpression. Dashed lines enclose oenocytes. N = 10 biological replicates. (L) *mElo*
943 expression in oenocytes following ISC-specific *Pvf1* overexpression. N = 4 biological
944 replicates from 2 independent experiments. (M-O) Immunostaining and qPCR analysis
945 reveal Hnf4 nuclear localization and *mElo* expression in oenocytes overexpressing active
946 *PvR*. Dashed lines enclose oenocytes in all immunostaining images. Data are presented as
947 mean ± s.e.m.; statistical significance was assessed using Student's t-test or ANOVA.
948

949 **Figure 3S: Expression of *Pvf1* in fly whole body and oenocytes in Yki flies.**
950 (A) Heatmap showing average gene expression changes (log2 fold change; Yki vs WT at day
951 8) across multiple tissues. (B) UMAP from whole body (without head) snRNAseq, shows
952 *Pvf1* expression level, oenocyte cluster is marked as "oe". (C) Ovary wasting of Yki flies with
953 ISC-specific *Pvf1* knockdown. Dashed lines enclose oenocytes. N = 10-20 biological
954 replicates. (D) Tumor mass (GFP-positive region of the gut) in Yki flies with ISC-specific *Pvf1*
955 knockdown. N = 8-10 biological replicates. (E) Ovary wasting of Yki flies with ISC-specific
956 *Pvf1* knockdown. Dashed lines enclose oenocytes. N = 10-20 biological replicates. (F)

957 Tumor mass (GFP-positive region of the gut) in Yki flies with ISC-specific *Pvf1* knockdown.
958 N = 8-10 biological replicates.
959
960 **Figure 4: Circulating lipids target trachea but not ISCs to promote tracheal growth.**
961 (A) Untargeted lipidomic analysis of fly hemolymph showing lipid species in control, Yki
962 flies, and Yki flies with oenocyte-specific *Hnf4* knockdown (*Esg>yki$^{3SA}$;PromE>Hnf4-i*). N = 4
963 biological replicates. (B-C) Levels of very-long-acylcarnitines (AcCa 24:1 and AcCa 24:2) in
964 Yki flies with or without *Hnf4* knockdown in oenocytes. (D-E) Levels of circulating
965 phospholipids, including PC 36:4 PE 32:5, across experimental conditions. (F-G) Levels of
966 circulating TG 18:3_16:0_16:1 and TG 18:2_16:0_18:0 in the fly hemolymph. (H-J) Number
967 of tracheal branches, tube area, and skeleton length in Yki flies with ISC-specific
968 knockdown of *LpR1* and *LpR2*. (K) PH3+ cell counts in ISCs of Yki flies with ISC-specific
969 knockdown of *LpR1* and *LpR2*. (L) PH3+ cell counts in ISCs of Yki flies with trachea-specific
970 (*Btl-Gal4* driver) knockdown of *LpR1* and *LpR2*. (M) GFP positive region in the gut of tracheal
971 specific *LpR2* knockdown in Yki flies. N = 8-12 flies. (N) Abdominal bloating area in Yki flies
972 with trachea-specific LpR2 knockdown. (O-Q) Number of tracheal branches, tube area,
973 and skeleton length in Yki flies with trache-specific knockdown of *LpR2*. N = 8-12. Data are
974 presented as mean ± s.e.m.; statistical analysis was performed using Student's t-test or
975 ANOVA as appropriate.
976
977 **Figure 4S: Effects of ISC-specific *LpR1* and *LpR2* knockdown on tracheal morphology**
978 **and ISC proliferation.**
979 (A) Counts of pH3+ cells in the midgut of flies with oenocyte-specific *TSC1*,2
980 overexpression or *Hnf4* knockdown or overexpression. N = 8-20 flies. (B-D) Trachea
981 parameters, including number of branches, tube area, and skeleton length, in flies with
982 ISC-specific knockdown of *LpR1* and *LpR2* using *Esg* driver, compared to control (*Esg>ctrl*).
983 N = 7-11 flies. (E) Counts of pH3+ cells in the midgut of flies with ISC-specific knockdown of
984 *LpR1* and *LpR2*, compared to controls. (F) *LpR1* expression level in fly thoraces with *LpR1*
985 knockdown using temperature sensitive muscle specific driver (Mhc-Gal4) activated at

986 adult stage for 7 days. (G) *LpR2* expression level in fly fat bodies with *LpR2* knockdown
987 using temperature sensitive fat body specific driver (Lpp-Gal4) activated at adult stage for 7
988 days. (H-J) Gut tracheal parameters in flies with oenocyte-specific *LpR2* knockdown.
989 N=20-25 flies. Data are presented as mean ± s.e.m.; statistical analysis was performed
990 using Student's t-test or ANOVA as appropriate.
991
992 **Figure 5: Hnf4-mElo axis in oenocytes mediates lipid metabolism and tracheogenesis**
993 **induced by Yki tumors.**
994 (A-C) Number of tracheal branches, total tube area, and total tube length in the midgut of
995 Yki flies with oenocyte-specific *TSC1,2* overexpression, *Hnf4* knockdown, or *mElo*
996 knockdown. N = 9-17 flies. (D-F) Tracheal morphology measurements, including number of
997 branches and skeleton length, in flies with ISC-specific knockdown of *Pvf1* combined with
998 *yki* overexpression (*Esg>yki*$^{3SA}$*;Pvf1-i*). N = 9-11 flies. Dashed lines enclose oenocytes in all
999 relevant images. Data are presented as mean ± s.e.m.; statistical analysis was performed
1000 using Student's t-test or ANOVA as appropriate.
1001
1002 **Figure 5S: Hnf4-mElo axis in oenocytes mediates lipid metabolism and tracheogenesis**
1003 **induced by Yki tumors.**
1004 (A-D) Tracheal morphology parameters, including number of branches, total tube area,
1005 total tube length, and skeleton length, in Yki midgut (*Esg>yki*), compared to wild-type
1006 controls (*Esg>ctrl*). N = 16-17.
1007
1008 **Figure 6: Hnf4-mElo axis regulates tracheogenesis in the midgut.**
1009 (A-B) Whole-body wax ester (WE) levels in flies with oenocyte-specific *Hnf4* knockdown
1010 (*PromE*$^{gs}$*>Hnf4-i*), *mElo* knockdown (*PromE*$^{gs}$*>mElo-i*), or *TSC1,2* overexpression
1011 (*PromE*$^{gs}$*>TSC1,2*). N = 3-4 biological replicates (C) Transepithelial barrier function of the
1012 trachea on the midgut, assessed using red dextran injection, in flies with oenocyte-specific
1013 *Hnf4* knockdown. N = 8 flies. (D-G) Trachea morphology on the midgut (R2-R4), including
1014 branch number and skeleton length normalized to gut surface area, in flies with *Hnf4*

knockdown in oenocytes. N = 8 flies. (H-J) Branch number, tube area, and skeleton length of the midgut trachea in flies with oenocyte-specific *mElo* knockdown. N = 6-8 flies (K-P) Number of branches, tracheal tube area and skeleton length of the midgut in flies overexpressing *Hnf4* or *mElo* in oenocytes (*PromE*$^{gs}$>*Hnf4* or *PromE*$^{gs}$>*mElo*). N = 8-15 flies.

**Figure 6S: Effect of oenocyte Hnf4 on ovary trachea.**

(A-D) Tracheal branch number, tube area and total skeleton length of the ovary in flies with *Hnf4* knockdown in oenocytes. Red (mtdTomato) marks the trachea (QF6>QUAS-mtdTomato). N = 8 flies. (E-G) Tracheal parameters of mid gut in flies with *Hnf4* knockdown in the fat body and gut. (N =18). (H-J) Tracheal parameters of mid gut in flies with *mElo* knockdown in the fat body and gut. (N =18). (K-M) Comparison of gut trachea morphology in control flies (*PromE*$^{gs}$>+) with and without RU feeding. N = 12 flies. Data are presented as mean ± s.e.m.; statistical analysis was performed using Student's t-test or ANOVA as appropriate.

**Figure 7: Regulation of hepatocyte lipid metabolism by pro-angiogenic factor in KL mice tumor model.**

(A-F) Relative expression levels of *ELOVL* fatty acid elongase 1,2,4, 6 and 7 and *APOB* in HepG2 cells incubated with vascular endothelial growth factor A (VEGF-A) for 24 hours, compared to controls. N = 4 biological replicates, from 2 independent experiments. (G) The level of WE from conditioned medium collected from HepG2 cultures following VEGF-A treatment. (H-L) Relative expression levels of *Hnf4α, Elovl7, Acc1* and *Fasn* in liver samples from *KrasG12D/+;Lkb1f/f* (KL) tumor-bearing mice compared to control mice. N = 3 biological replicates, from 2 independent experiments. (M) The level of WEs from serum samples of KL mice and control mice. (N) Heatmap showing the significantly changed lipid species from serum samples of tumor-bearing and control mice. (H) Schematic representation of the proposed mechanism, depicting tumor-secreted PDGF/VEGF-like factors activating the mTOR-Hnf4 axis in hepatocyte-like oenocytes to promote lipid synthesis, which are then transported to trachea. Data are presented as mean ± s.e.m.;

statistical analysis was performed using Student's t-test and significance analysis of microarrays was used for lipid species.

**Figure 7S: VEGF-A regulates lipid metabolism in hepatocytes.**

(A-B) Immunostaining of HepG2 cells treated with or without VEGF-A for 24 hours with Hnf4α and quantification of Hnf4α intensity in the nucleus, blue color indicates DAPI signal, scale bar represents 20μm. (C) The level of WEs with various fatty acid chain length in the serum of tumor bearing or control mice. (D) Heatmap showing the significantly altered lipid species from the serum of control and tumor bearing mice. Data are presented as mean ± s.e.m.; statistical analysis was performed using Student's t-test, and significance analysis of microarrays was used for (D).

## References


1. Bakopoulos, D., et al., *Convergent insulin and TGF-β signalling drives cancer cachexia by promoting aberrant fat body ECM accumulation in a Drosophila tumour model*. The EMBO Reports, 2023. **24**(12): p. EMBR202357695.
2. Fukumura, D., et al., *Tumor induction of VEGF promoter activity in stromal cells*. Cell, 1998. **94**(6): p. 715-25.
3. Quail, D.F. and J.A. Joyce, *Microenvironmental regulation of tumor progression and metastasis*. Nat Med, 2013. **19**(11): p. 1423-37.
4. Winkler, J., et al., *Concepts of extracellular matrix remodelling in tumour progression and metastasis*. Nat Commun, 2020. **11**(1): p. 5120.
5. Anderson, N.M. and M.C. Simon, *The tumor microenvironment*. Curr Biol, 2020. **30**(16): p. R921-r925.
6. Chen, X., et al., *Neural Circuitries between the Brain and Peripheral Solid Tumors*. Cancer Res, 2024. **84**(21): p. 3509-3521.
7. Goncalves, M.D., et al., *Fenofibrate prevents skeletal muscle loss in mice with lung cancer*. Proceedings of the National Academy of Sciences, 2018. **115**(4): p. E743-E752.
8. Schutz, Y., *Protein turnover, ureagenesis and gluconeogenesis*. Int J Vitam Nutr Res, 2011. **81**(2-3): p. 101-7.
9. Lee, J.S., et al., *Urea Cycle Dysregulation Generates Clinically Relevant Genomic and Biochemical Signatures*. Cell, 2018. **174**(6): p. 1559-1570 e22.
10. Al-Zoughbi, W. and G. Hoefler, *Tumor Macroenvironment: An Update*. Pathobiology, 2020. **87**(2): p. 58-60.

11. Goldman, O., et al., *Early Infiltration of Innate Immune Cells to the Liver Depletes HNF4alpha and Promotes Extrahepatic Carcinogenesis*. Cancer Discov, 2023. **13**(7): p. 1616-1635.
12. Liu, Y., et al., *Hepatic gluconeogenesis and PDK3 upregulation drive cancer cachexia in flies and mice*. Nat Metab, 2025. **7**(4): p. 823-841.
13. Grossberg, A.J., et al., *Interleukin 6-independent metabolic reprogramming as a driver of cancer-related fatigue*. Brain, Behavior, and Immunity, 2020. **88**: p. 230-241.
14. Fearon, K.C., et al., *Elevated circulating interleukin-6 is associated with an acute-phase response but reduced fixed hepatic protein synthesis in patients with cancer*. Ann Surg, 1991. **213**(1): p. 26-31.
15. Wang, G., et al., *Tumour extracellular vesicles and particles induce liver metabolic dysfunction*. Nature, 2023. **618**(7964): p. 374-382.
16. Jin, H.-R., et al., *Lipid metabolic reprogramming in tumor microenvironment: from mechanisms to therapeutics*. Journal of Hematology & Oncology, 2023. **16**(1): p. 103.
17. Wang, H., et al., *CD36-mediated metabolic adaptation supports regulatory T cell survival and function in tumors*. Nat Immunol, 2020. **21**(3): p. 298-308.
18. Wu, L., et al., *RIPK3 Orchestrates Fatty Acid Metabolism in Tumor-Associated Macrophages and Hepatocarcinogenesis*. Cancer Immunol Res, 2020. **8**(5): p. 710-721.
19. Veglia, F., et al., *Fatty acid transport protein 2 reprograms neutrophils in cancer*. Nature, 2019. **569**(7754): p. 73-78.
20. Patel, P.H. and B.A. Edgar, *Tissue design: How Drosophila tumors remodel their neighborhood*. Seminars in Cell & Developmental Biology, 2014. **28**: p. 86-95.
21. Kwon, Y., et al., *Systemic organ wasting induced by localized expression of the secreted insulin/IGF antagonist ImpL2*. Dev Cell, 2015. **33**(1): p. 36-46.
22. Song, W., et al., *Tumor-Derived Ligands Trigger Tumor Growth and Host Wasting via Differential MEK Activation*. Dev Cell, 2019. **48**(2): p. 277-286 e6.
23. Konishi, T., et al., *The K-ras gene regulates vascular endothelial growth factor gene expression in non-small cell lung cancers*. Int J Oncol, 2000. **16**(3): p. 501-11.
24. Sunaga, N., et al., *Targeting Oncogenic KRAS in Non-Small-Cell Lung Cancer*. Cancers (Basel), 2021. **13**(23).
25. Brooks, G.D., et al., *IL6 Trans-signaling Promotes KRAS-Driven Lung Carcinogenesis*. Cancer Res, 2016. **76**(4): p. 866-76.
26. Olivares-Hernández, A., et al., *Current and future perspectives in clinical practice in KRAS-mutated non-small cell lung cancer: a literature review*. Precision Cancer Medicine, 2024. **7**.
27. Bilder, D., et al., *Tumour-host interactions through the lens of Drosophila*. Nat Rev Cancer, 2021. **21**(11): p. 687-700.
28. Droujinine, I.A. and N. Perrimon, *Interorgan Communication Pathways in Physiology: Focus on Drosophila*. Annu Rev Genet, 2016. **50**: p. 539-570.
29. Gutierrez, E., et al., *Specialized hepatocyte-like cells regulate Drosophila lipid metabolism*. Nature, 2007. **445**(7125): p. 275-80.

1123 30. Chatterjee, D., et al., *Control of metabolic adaptation to fasting by dILP6-induced*
1124 *insulin signaling in Drosophila oenocytes*. Proc Natl Acad Sci U S A, 2014. **111**(50):
1125 p. 17959-64.
1126 31. Billeter, J.C., et al., *Specialized cells tag sexual and species identity in Drosophila*
1127 *melanogaster*. Nature, 2009. **461**(7266): p. 987-91.
1128 32. Ferveur, J.F., et al., *Genetic feminization of pheromones and its behavioral*
1129 *consequences in Drosophila males*. Science, 1997. **276**(5318): p. 1555-8.
1130 33. Blomquist, G.J., A.J. Chu, and S. Remaley, *Biosynthesis of wax in the honeybee, Apis*
1131 *mellifera L*. Insect Biochemistry, 1980. **10**(3): p. 313-321.
1132 34. Qiu, Y., et al., *An insect-specific P450 oxidative decarbonylase for cuticular*
1133 *hydrocarbon biosynthesis*. Proc Natl Acad Sci U S A, 2012. **109**(37): p. 14858-63.
1134 35. Reed, J.R., et al., *Unusual mechanism of hydrocarbon formation in the housefly:*
1135 *cytochrome P450 converts aldehyde to the sex pheromone component (Z)-9-*
1136 *tricosene and CO2*. Proceedings of the National Academy of Sciences, 1994. **91**(21):
1137 p. 10000-10004.
1138 36. Wicker-Thomas, C., et al., *Flexible origin of hydrocarbon/pheromone precursors in*
1139 *Drosophila melanogaster*. J Lipid Res, 2015. **56**(11): p. 2094-101.
1140 37. Wang, Z., et al., *Evolution of a fatty acyl-CoA elongase underlies desert adaptation in*
1141 *Drosophila*. Sci Adv, 2023. **9**(35): p. eadg0328.
1142 38. Labeur, C., R. Dallerac, and C. Wicker-Thomas, *Involvement of desat1 gene in the*
1143 *control of Drosophila melanogaster pheromone biosynthesis*. Genetica, 2002.
1144 **114**(3): p. 269-74.
1145 39. Storelli, G., et al., *Drosophila HNF4 Directs a Switch in Lipid Metabolism that*
1146 *Supports the Transition to Adulthood*. Dev Cell, 2019. **48**(2): p. 200-214 e6.
1147 40. Ghabrial, A., et al., *Branching morphogenesis of the Drosophila tracheal system*.
1148 Annu Rev Cell Dev Biol, 2003. **19**: p. 623-47.
1149 41. Li, Z., et al., *Trachea-derived dpp controls adult midgut homeostasis in Drosophila*.
1150 Dev Cell, 2013. **24**(2): p. 133-43.
1151 42. Tamamouna, V., et al., *Remodelling of oxygen-transporting tracheoles drives*
1152 *intestinal regeneration and tumorigenesis in Drosophila*. Nat Cell Biol, 2021. **23**(5):
1153 p. 497-510.
1154 43. Perochon, J., et al., *Dynamic adult tracheal plasticity drives stem cell adaptation to*
1155 *changes in intestinal homeostasis in Drosophila*. Nat Cell Biol, 2021. **23**(5): p. 485-
1156 496.
1157 44. Kwon, Y., et al., *Systemic Organ Wasting Induced by Localized Expression of the*
1158 *Secreted Insulin/IGF Antagonist ImpL2*. Developmental Cell, 2015. **33**(1): p. 36-46.
1159 45. Patel, S., D.R. Nelson, and A.G. Gibbs, *Chemical and physical analyses of wax ester*
1160 *properties*. J Insect Sci, 2001. **1**: p. 4.
1161 46. Palanker, L., et al., *Drosophila HNF4 Regulates Lipid Mobilization and β-Oxidation*.
1162 Cell Metabolism, 2009. **9**(3): p. 228-239.
1163 47. Xu, J., et al., *Protein visualization and manipulation in Drosophila through the use of*
1164 *epitope tags recognized by nanobodies*. eLife, 2022. **11**: p. e74326.

48. Bradley, M.E., et al., *Potent and Efficacious Inhibition of CXCR2 Signaling by Biparatopic Nanobodies Combining Two Distinct Modes of Action*. Molecular Pharmacology, 2015. **87**(2): p. 251-262.
49. Palanker, L., et al., *Drosophila HNF4 regulates lipid mobilization and beta-oxidation*. Cell Metab, 2009. **9**(3): p. 228-39.
50. Ghosh, A.C., et al., *Drosophila PDGF/VEGF signaling from muscles to hepatocyte-like cells protects against obesity*. eLife, 2020. **9**: p. e56969.
51. Zhang, Y., et al., *Rheb is a direct target of the tuberous sclerosis tumour suppressor proteins*. Nature Cell Biology, 2003. **5**(6): p. 578-581.
52. Sopko, R., et al., *A systems-level interrogation identifies regulators of Drosophila blood cell number and survival*. PLoS Genet, 2015. **11**(3): p. e1005056.
53. Tran, T.A., et al., *Platelet-derived growth factor/vascular endothelial growth factor receptor inactivation by sunitinib results in Tsc1/Tsc2-dependent inhibition of TORC1*. Mol Cell Biol, 2013. **33**(19): p. 3762-79.
54. Cruciani, G., et al., *Diagnostic application of lipidomics fingerprints to bladder carcinoma*. Translational Cancer Research, 2017. **6**(6): p. 1197-1206.
55. Simcox, J., et al., *Global Analysis of Plasma Lipids Identifies Liver-Derived Acylcarnitines as a Fuel Source for Brown Fat Thermogenesis*. Cell Metabolism, 2017. **26**(3): p. 509-522.e6.
56. Palm, W., et al., *Lipoproteins in Drosophila melanogaster--assembly, function, and influence on tissue lipid composition*. PLoS Genet, 2012. **8**(7): p. e1002828.
57. Vonolfen, M.C., et al., *Drosophila HNF4 acts in distinct tissues to direct a switch between lipid storage and export in the gut*. Cell Rep, 2024. **43**(9): p. 114693.
58. Khaliullina, H., et al., *Patched regulates Smoothened trafficking using lipoprotein-derived lipids*. Development, 2009. **136**(24): p. 4111-21.
59. Locke, M., *Pore canals and related structures in insect cuticle*. J Biophys Biochem Cytol, 1961. **10**(4): p. 589-618.
60. Moussian, B., *Recent advances in understanding mechanisms of insect cuticle differentiation*. Insect Biochem Mol Biol, 2010. **40**(5): p. 363-75.
61. Moussian, B., et al., *Cuticle differentiation during Drosophila embryogenesis*. Arthropod Struct Dev, 2006. **35**(3): p. 137-52.
62. Jaspers, M.H., et al., *The fatty acyl-CoA reductase Waterproof mediates airway clearance in Drosophila*. Dev Biol, 2014. **385**(1): p. 23-31.
63. Chatterjee, N. and N. Perrimon, *What fuels the fly: Energy metabolism in Drosophila and its application to the study of obesity and diabetes*. Science Advances, 2021. **7**(24): p. eabg4336.
64. Huang, K., et al., *RiboTag translatomic profiling of Drosophila oenocytes under aging and induced oxidative stress*. BMC Genomics, 2019. **20**(1): p. 50.
65. Rera, M., et al., *Modulation of longevity and tissue homeostasis by the Drosophila PGC-1 homolog*. Cell Metab, 2011. **14**(5): p. 623-34.
66. Radi, S.H., et al., *HNF4alpha isoforms: the fraternal twin master regulators of liver function*. Front Endocrinol (Lausanne), 2023. **14**: p. 1226173.

1207 67. Metzger, S., et al., *Orphan receptor HNF-4 and bZip protein C/EBP alpha bind to*
1208 *overlapping regions of the apolipoprotein B gene promoter and synergistically*
1209 *activate transcription*. J Biol Chem, 1993. **268**(22): p. 16831-8.
1210 68. Adamson, A.W., et al., *Hepatocyte nuclear factor-4alpha contributes to*
1211 *carbohydrate-induced transcriptional activation of hepatic fatty acid synthase*.
1212 Biochem J, 2006. **399**(2): p. 285-95.
1213 69. Meng, J., et al., *Identification of HNF-4α as a key transcription factor to promote*
1214 *ChREBP expression in response to glucose*. Scientific Reports, 2016. **6**(1): p. 23944.
1215 70. Bideyan, L., R. Nagari, and P. Tontonoz, *Hepatic transcriptional responses to fasting*
1216 *and feeding*. Genes Dev, 2021. **35**(9-10): p. 635-657.
1217 71. Ding, G., et al., *Coordination of tumor growth and host wasting by tumor-derived*
1218 *Upd3*. Cell Rep, 2021. **36**(7): p. 109553.
1219 72. Xu, J., et al., *Mechanistic characterization of a Drosophila model of paraneoplastic*
1220 *nephrotic syndrome*. Nature Communications, 2024. **15**(1): p. 1241.
1221 73. Duvel, K., et al., *Activation of a metabolic gene regulatory network downstream of*
1222 *mTOR complex 1*. Mol Cell, 2010. **39**(2): p. 171-83.
1223 74. Tiebe, M., et al., *REPTOR and REPTOR-BP Regulate Organismal Metabolism and*
1224 *Transcription Downstream of TORC1*. Dev Cell, 2015. **33**(3): p. 272-84.
1225 75. Hoch, R.V. and P. Soriano, *Roles of PDGF in animal development*. Development,
1226 2003. **130**(20): p. 4769-84.
1227 76. Holmes, D.I. and I. Zachary, *The vascular endothelial growth factor (VEGF) family:*
1228 *angiogenic factors in health and disease*. Genome Biol, 2005. **6**(2): p. 209.
1229 77. Jiang, H., et al., *Cytokine/Jak/Stat signaling mediates regeneration and homeostasis*
1230 *in the Drosophila midgut*. Cell, 2009. **137**(7): p. 1343-55.
1231 78. Buchon, N., et al., *Drosophila intestinal response to bacterial infection: activation of*
1232 *host defense and stem cell proliferation*. Cell Host Microbe, 2009. **5**(2): p. 200-11.
1233 79. Apidianakis, Y., et al., *Synergy between bacterial infection and genetic*
1234 *predisposition in intestinal dysplasia*. Proc Natl Acad Sci U S A, 2009. **106**(49): p.
1235 20883-8.
1236 80. Amcheslavsky, A., et al., *Enteroendocrine Cells Support Intestinal Stem-Cell-*
1237 *Mediated Homeostasis in Drosophila*. Cell Reports, 2014. **9**(1): p. 32-39.
1238 81. Lin, G., N. Xu, and R. Xi, *Paracrine Wingless signalling controls self-renewal of*
1239 *Drosophila intestinal stem cells*. Nature, 2008. **455**(7216): p. 1119-1123.
1240 82. Schönfeld, P. and G. Reiser, *Brain Lipotoxicity of Phytanic Acid and Very Long-chain*
1241 *Fatty Acids. Harmful Cellular/Mitochondrial Activities in Refsum Disease and X-*
1242 *Linked Adrenoleukodystrophy*. Aging Dis, 2016. **7**(2): p. 136-49.
1243 83. Baarine, M., et al., *Evidence of oxidative stress in very long chain fatty acid--treated*
1244 *oligodendrocytes and potentialization of ROS production using RNA interference-*
1245 *directed knockdown of ABCD1 and ACOX1 peroxisomal proteins*. Neuroscience,
1246 2012. **213**: p. 1-18.
1247 84. Zarrouk, A., et al., *Induction of mitochondrial changes associated with oxidative*
1248 *stress on very long chain fatty acids (C22:0, C24:0, or C26:0)-treated human*
1249 *neuronal cells (SK-NB-E)*. Oxid Med Cell Longev, 2012. **2012**: p. 623257.

85. Sargent, J.R., R.R. Gatten, and R. McIntosh, *Wax esters in the marine environment — their occurrence, formation, transformation and ultimate fates*. Marine Chemistry, 1977. **5**(4): p. 573-584.
86. Rosca, M.G., et al., *Oxidation of Fatty Acids Is the Source of Increased Mitochondrial Reactive Oxygen Species Production in Kidney Cortical Tubules in Early Diabetes*. Diabetes, 2012. **61**(8): p. 2074-2083.
87. Tamura, K., et al., *Novel lipogenic enzyme ELOVL7 is involved in prostate cancer growth through saturated long-chain fatty acid metabolism*. Cancer Res, 2009. **69**(20): p. 8133-40.
88. Karlsson, M., et al., *A single–cell type transcriptomics map of human tissues*. Science Advances, 2021. **7**(31): p. eabh2169.
89. Hirota, K., et al., *A Combination of HNF-4 and Foxo1 Is Required for Reciprocal Transcriptional Regulation of Glucokinase and Glucose-6-phosphatase Genes in Response to Fasting and Feeding *<sup></sup>*. Journal of Biological Chemistry, 2008. **283**(47): p. 32432-32441.
90. Koyama, T. and C.K. Mirth, *Growth-Blocking Peptides As Nutrition-Sensitive Signals for Insulin Secretion and Body Size Regulation*. PLoS Biol, 2016. **14**(2): p. e1002392.
91. Pallares-Cartes, C., G. Cakan-Akdogan, and Aurelio A. Teleman, *Tissue-Specific Coupling between Insulin/IGF and TORC1 Signaling via PRAS40 in Drosophila*. Developmental Cell, 2012. **22**(1): p. 172-182.
92. Chatterjee, D., et al., *Control of metabolic adaptation to fasting by dILP6-induced insulin signaling in Drosophila oenocytes*. Proceedings of the National Academy of Sciences, 2014. **111**(50): p. 17959-17964.
93. Chung, H., et al., *A Single Gene Affects Both Ecological Divergence and Mate Choice in Drosophila*. Science, 2014. **343**(6175): p. 1148-1151.
94. Wang, Z., et al., *Evolution of a fatty acyl–CoA elongase underlies desert adaptation in Drosophila*. Science Advances, 2023. **9**(35): p. eadg0328.
95. Montoya-Zegarra, J.A., et al., *AutoTube: a novel software for the automated morphometric analysis of vascular networks in tissues*. Angiogenesis, 2019. **22**(2): p. 223-236.
96. Ji, H., et al., *LKB1 modulates lung cancer differentiation and metastasis*. Nature, 2007. **448**(7155): p. 807-810.

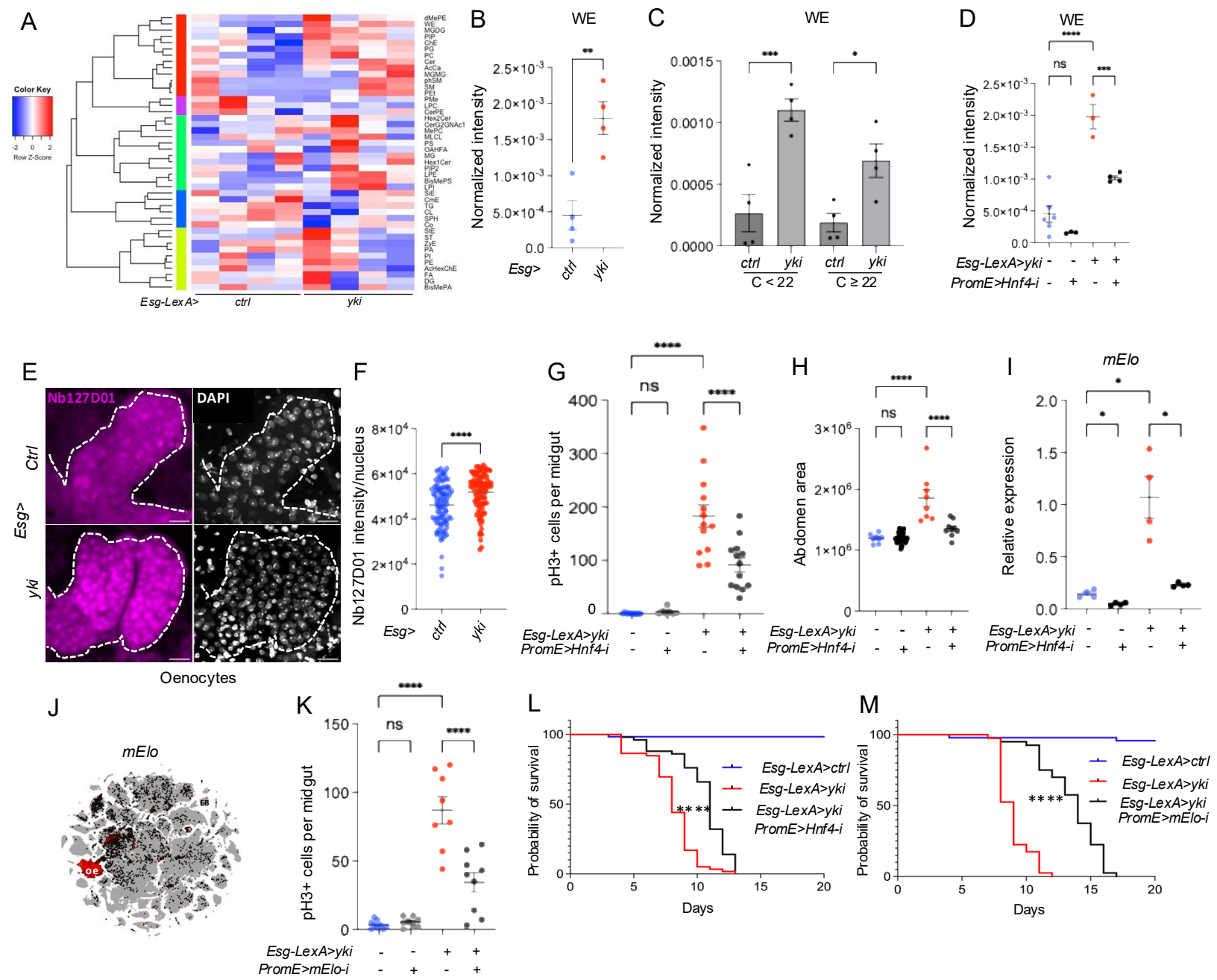
A
Color Key
Row Z-Score
Esg-LexA>
ctrl
yki
B
WE
Normalized intensity
Esg>
ctrl
yki
C
WE
Normalized intensity
ctrl
yki
C < 22
C ≥ 22
D
WE
Normalized intensity
Esg-LexA>yki
PromE>Hnf4-i
E
Nb127D01
DAPI
Ctrl
Esg>
yki
Oenocytes
F
Nb127D01 intensity/nucleus
Esg>
ctrl
yki
G
pH3+ cells per midgut
Esg-LexA>yki
PromE>Hnf4-i
H
Abdomen area
Esg-LexA>yki
PromE>Hnf4-i
I
mElo
Relative expression
Esg-LexA>yki
PromE>Hnf4-i
J
mElo
EB
oe
K
pH3+ cells per midgut
Esg-LexA>yki
PromE>mElo-i
L
Probability of survival
Days
Esg-LexA>ctrl
Esg-LexA>yki
Esg-LexA>yki
PromE>Hnf4-i
M
Probability of survival
Days
Esg-LexA>ctrl
Esg-LexA>yki
Esg-LexA>yki
PromE>mElo-i

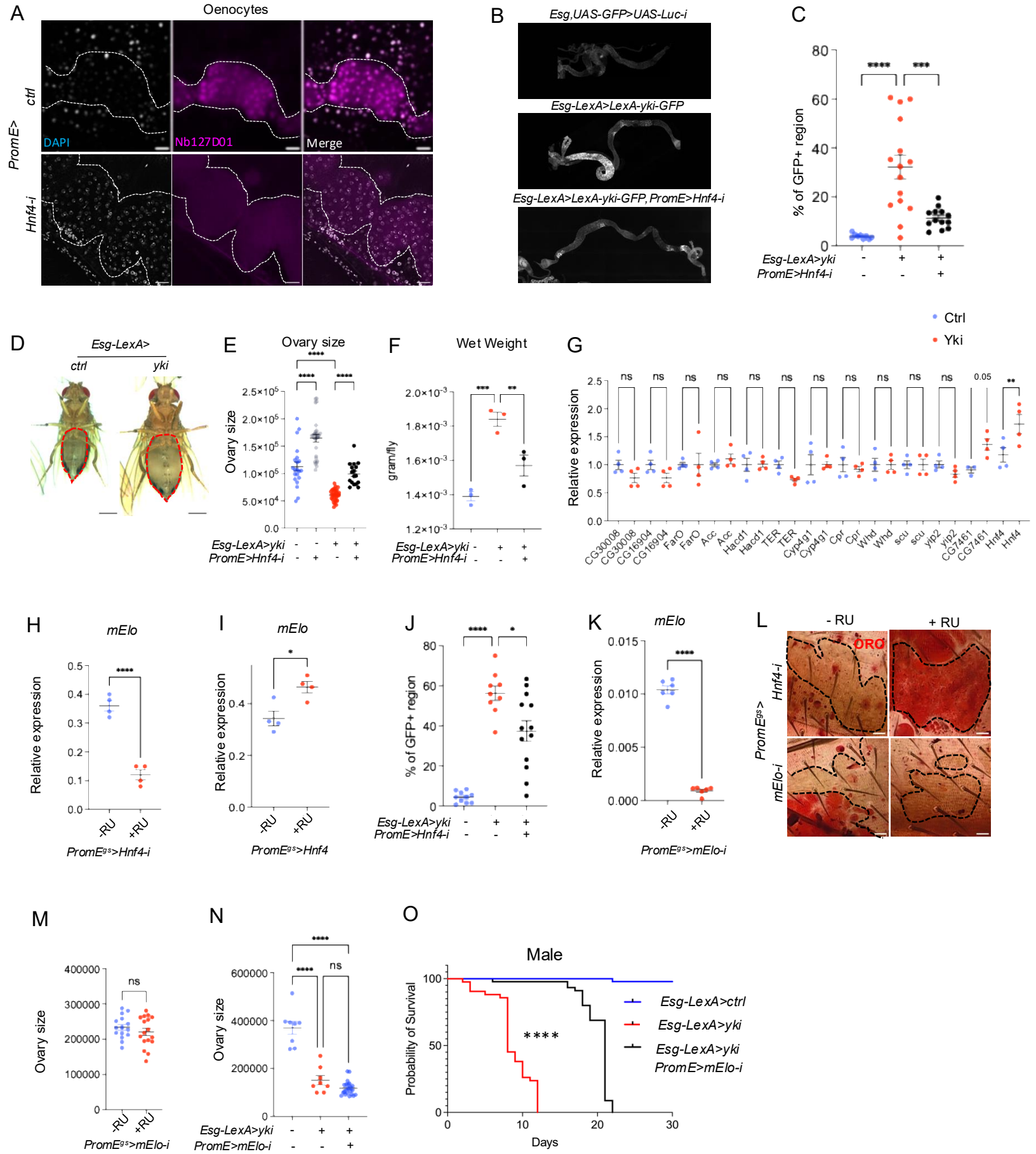
A
Oenocytes
PromE>
ctrl
Hnf4-i
DAPI
Nb127D01
Merge
B
Esg,UAS-GFP>UAS-Luc-i
Esg-LexA>LexA-yki-GFP
Esg-LexA>LexA-yki-GFP, PromE>Hnf4-i
C
% of GFP+ region
Esg-LexA>yki
PromE>Hnf4-i
D
Esg-LexA>
ctrl
yki
E
Ovary size
Ovary size
Esg-LexA>yki
PromE>Hnf4-i
F
Wet Weight
gram/fly
Esg-LexA>yki
PromE>Hnf4-i
G
Ctrl
Yki
Relative expression
CG30008
CG16904
FarO
Acc
Hacd1
TER
Cyp4g1
Cpr
Whd
scu
yip2
CG7461
Hnf4
H
mElo
Relative expression
-RU
+RU
PromEgs>Hnf4-i
I
mElo
Relative expression
-RU
+RU
PromEgs>Hnf4
J
% of GFP+ region
Esg-LexA>yki
PromE>Hnf4-i
K
mElo
Relative expression
-RU
+RU
PromEgs>mElo-i
L
- RU
+ RU
ORO
PromEgs>
Hnf4-i
mElo-i
M
Ovary size
ns
-RU
+RU
PromEgs>mElo-i
N
Ovary size
ns
Esg-LexA>yki
PromE>mElo-i
O
Male
Probability of Survival
Days
Esg-LexA>ctrl
Esg-LexA>yki
Esg-LexA>yki
PromE>mElo-i

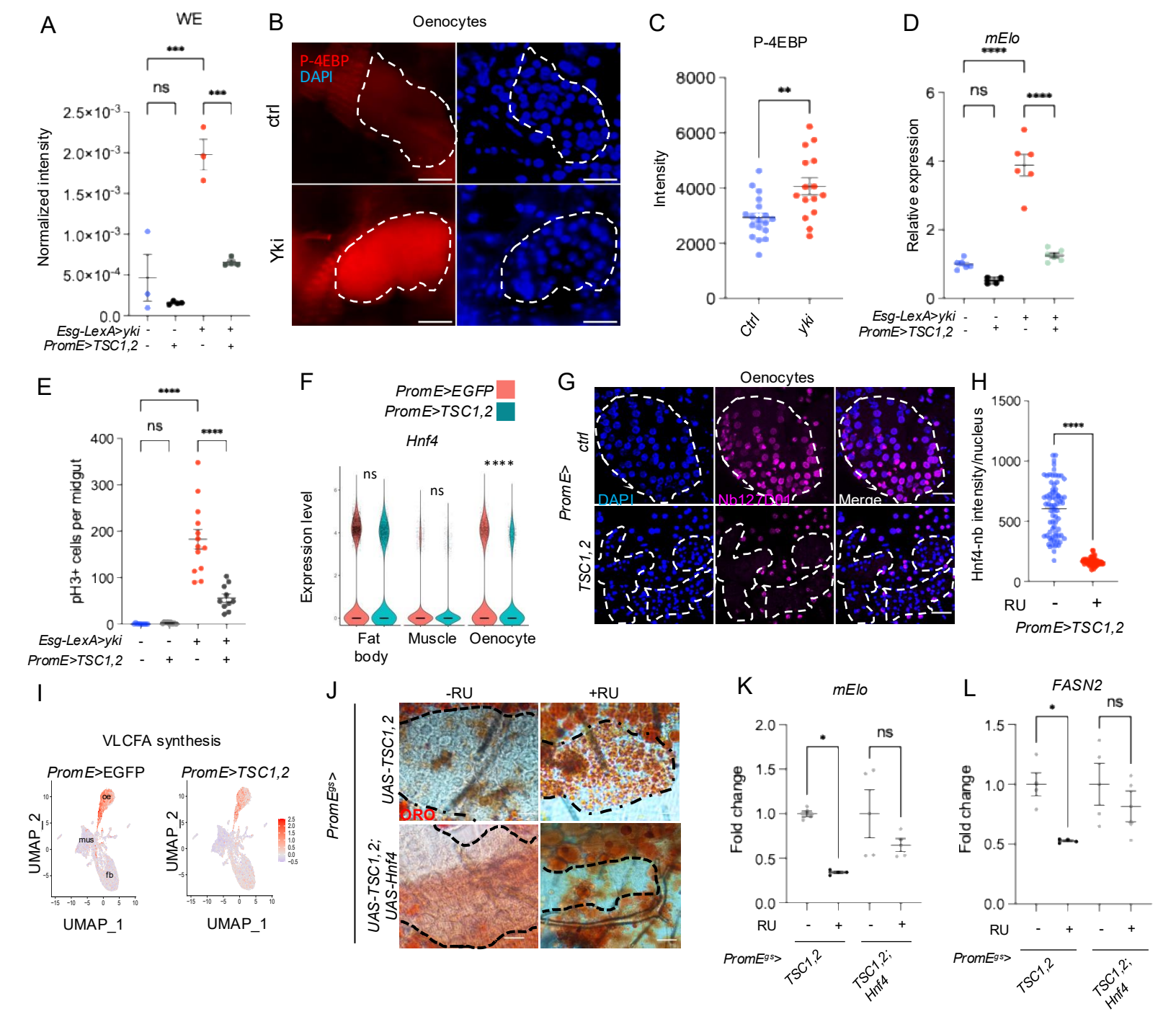
A
WE
Normalized intensity
ns
***
Esg-LexA>yki
PromE>TSC1,2
B
Oenocytes
P-4EBP
DAPI
ctrl
Yki
C
P-4EBP
Intensity
**
Ctrl
yki
D
mElo
Relative expression
ns
****
Esg-LexA>yki
PromE>TSC1,2
E
pH3+ cells per midgut
ns
****
Esg-LexA>yki
PromE>TSC1,2
F
PromE>EGFP
PromE>TSC1,2
Hnf4
Expression level
ns
ns
****
Fat body
Muscle
Oenocyte
G
Oenocytes
PromE>
ctrl
TSC1,2
DAPI
Nb127D04
Merge
H
Hnf4-nb intensity/nucleus
****
RU
PromE>TSC1,2
I
VLCFA synthesis
PromE>EGFP
PromE>TSC1,2
UMAP_2
UMAP_1
oe
mus
fb
J
-RU
+RU
PromEgs>
UAS-TSC1,2
UAS-TSC1,2; UAS-Hnf4
ORO
K
mElo
Fold change
*
ns
RU
PromEgs>
TSC1,2
TSC1,2; Hnf4
L
FASN2
Fold change
*
ns
RU
PromEgs>
TSC1,2
TSC1,2; Hnf4

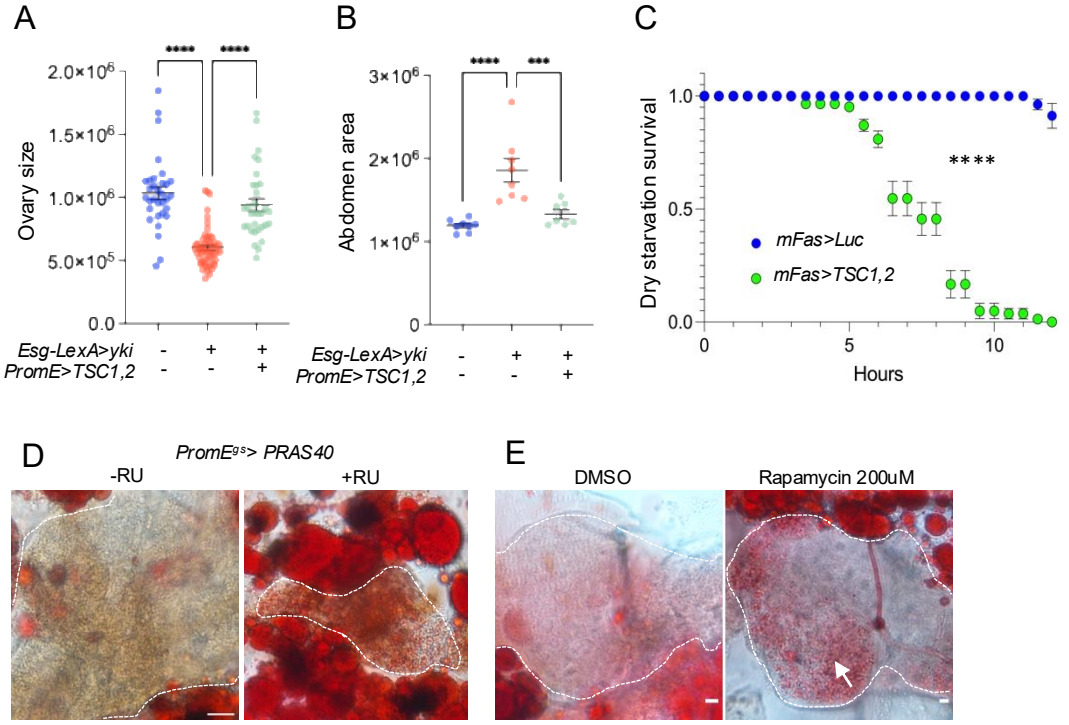
A
Ovary size
2.0×10^6
1.5×10^6
1.0×10^6
5.0×10^5
0.0
****
****
Esg-LexA>yki - + +
PromE>TSC1,2 - - +
B
Abdomen area
3×10^6
2×10^6
1×10^6
0
****
***
Esg-LexA>yki - + +
PromE>TSC1,2 - - +
C
Dry starvation survival
1.0
0.5
0.0
0
5
10
Hours
****
mFas>Luc
mFas>TSC1,2
D
PromE^gs> PRAS40
-RU
+RU
E
DMSO
Rapamycin 200uM

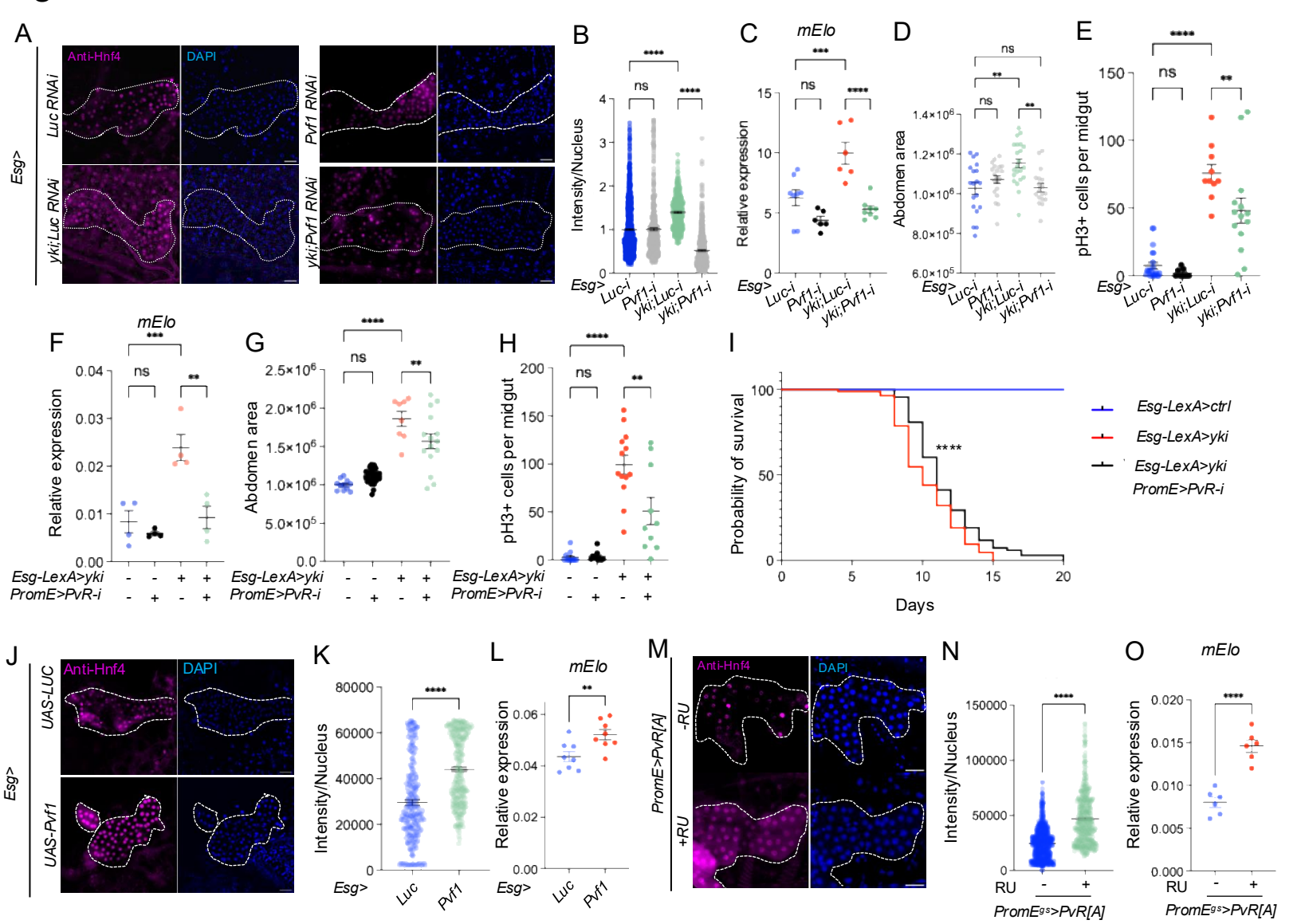
A
Anti-Hnf4
DAPI
Esg>
Luc RNAi
Pvf1 RNAi
yki;Luc RNAi
yki;Pvf1 RNAi
B
Intensity/Nucleus
C
mElo
Relative expression
D
Abdomen area
E
pH3+ cells per midgut
Esg>
Luc-i
Pvf1-i
yki;Luc-i
yki;Pvf1-i
F
mElo
Relative expression
G
Abdomen area
H
pH3+ cells per midgut
Esg-LexA>yki
PromE>PvR-i
I
Probability of survival
Days
Esg-LexA>ctrl
Esg-LexA>yki
Esg-LexA>yki
PromE>PvR-i


J
Anti-Hnf4
DAPI
Esg>
UAS-LUC
UAS-Pvf1
K
Intensity/Nucleus
L
mElo
Relative expression
Esg>
Luc
Pvf1
M
Anti-Hnf4
DAPI
PromE>PvR[A]
-RU
+RU
N
Intensity/Nucleus
O
mElo
Relative expression
RU
PromEgs>PvR[A]

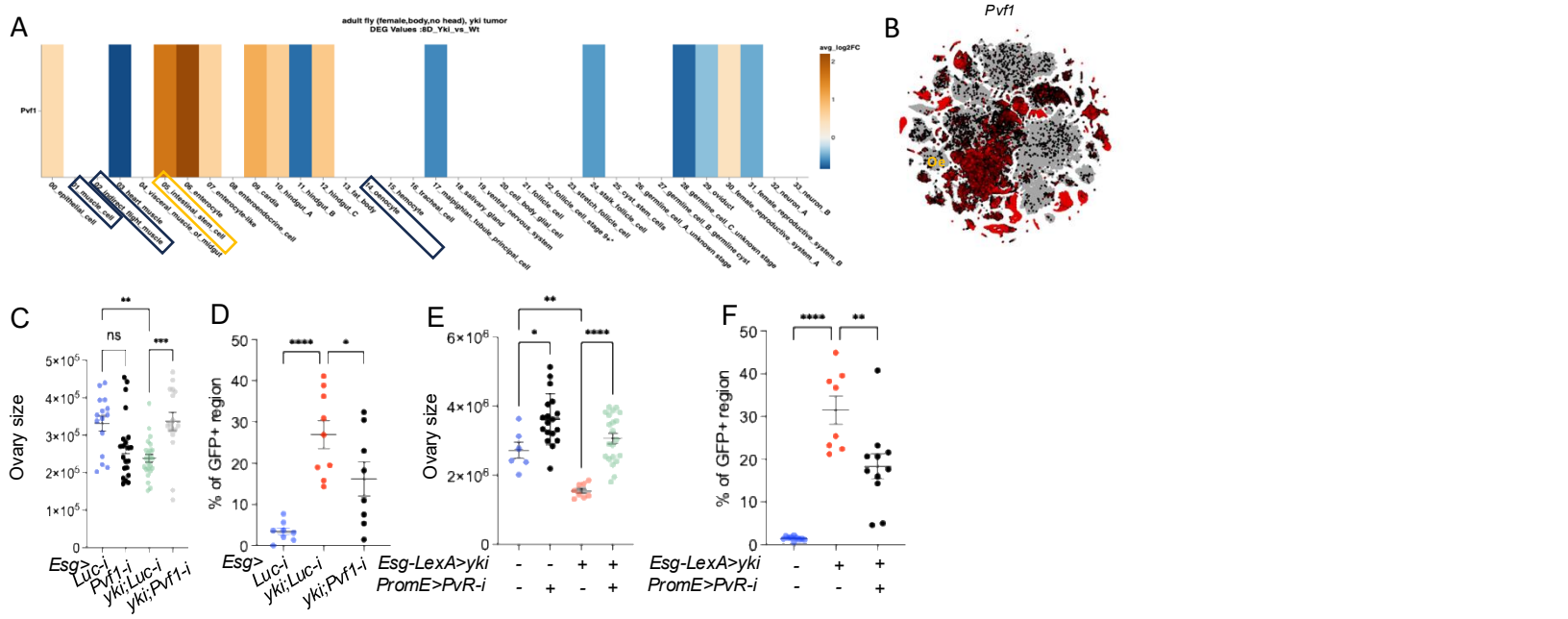
A
adult fly (female,body,no head), yki tumor
DEG Values :8D_Yki_vs_Wt
avg_log2FC
Pvf1
00_epithelial_cell
01_muscle_cell
02_indirect_flight_muscle
03_heart_muscle
04_visceral_muscle_of_midgut
05_intestinal_stem_cell
06_enterocyte
07_enterocyte-like
08_enteroendocrine_cell
09_cardia
10_hindgut_A
11_hindgut_B
12_hindgut_C
13_fat_body
14_oenocyte
15_hemocyte
16_tracheal_cell
17_malpighian_tubule_principal_cell
18_salivary_gland
19_ventral_nervous_system
20_cell_body_glial_cell
21_follicle_cell
22_follicle_cell_stage 9+
23_stretch_follicle_cell
24_stalk_follicle_cell
25_cyst_stem_cells
26_germline_cell_A_unknown stage
27_germline_cell_B_germline cyst
28_germline_cell_C_unknown stage
29_oviduct
30_female_reproductive_system_A
31_female_reproductive_system_B
32_neuron_A
33_neuron_B
B
Pvf1
C
Ovary size
ns
Esg>
Luc-i
Pvf1-i
yki;Luc-i
yki;Pvf1-i
D
% of GFP+ region
Esg>
Luc-i
yki;Luc-i
yki;Pvf1-i
E
Ovary size
Esg-LexA>yki
PromE>PvR-i
F
% of GFP+ region
Esg-LexA>yki
PromE>PvR-i

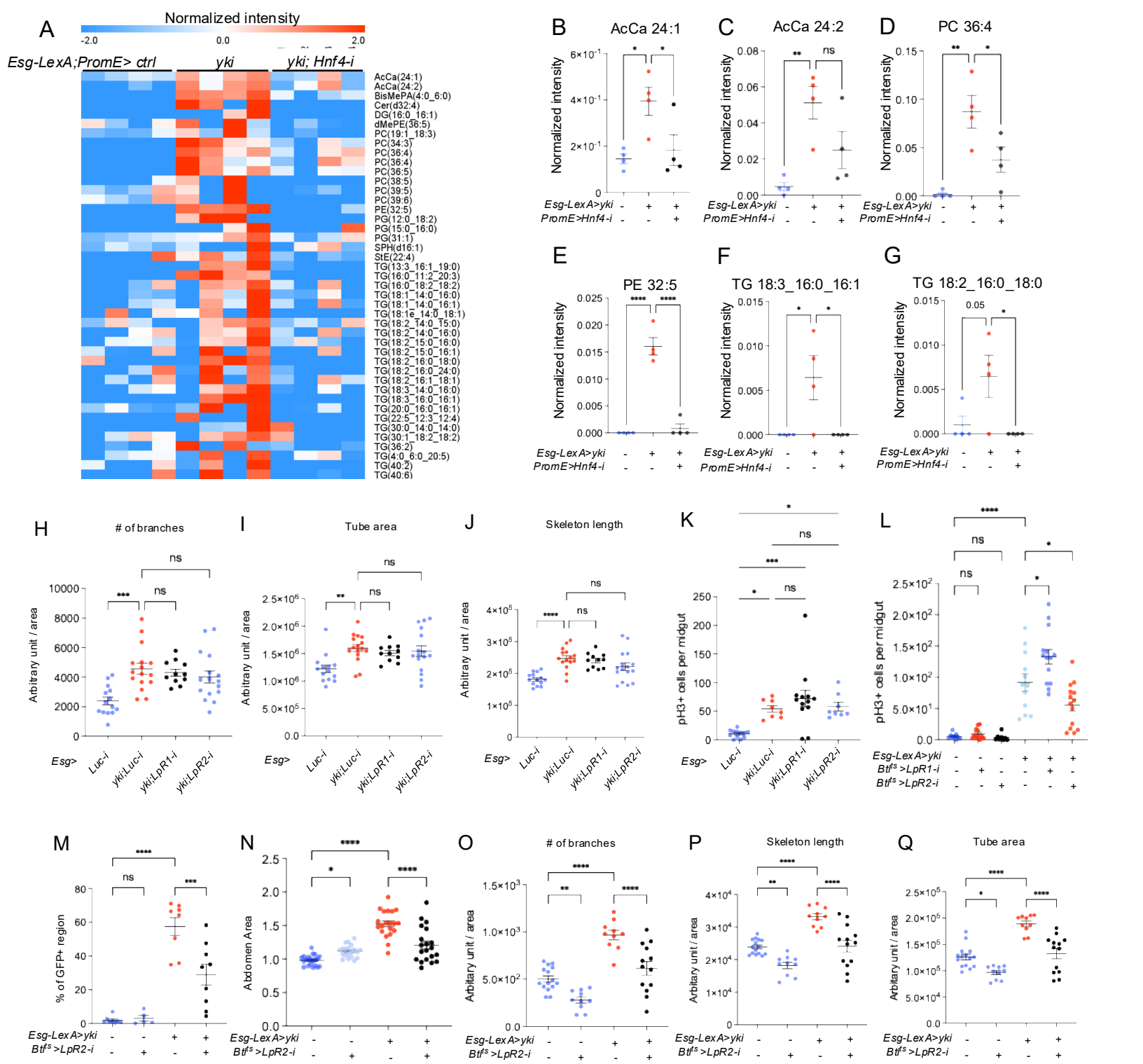
A
Normalized intensity
-2.0
0.0
2.0
Esg-LexA;PromE> ctrl
yki
yki; Hnf4-i
AcCa(24:1)
AcCa(24:2)
BisMePA(4:0_6:0)
Cer(d32:4)
DG(16:0_16:1)
dMePE(36:5)
PC(19:1_18:3)
PC(34:3)
PC(36:4)
PC(36:4)
PC(36:5)
PC(38:5)
PC(39:5)
PC(39:6)
PE(32:5)
PG(12:0_18:2)
PG(15:0_16:0)
PG(31:1)
SPH(d16:1)
StE(22:4)
TG(13:3_16:1_19:0)
TG(16:0_11:2_20:3)
TG(16:0_18:2_18:2)
TG(18:1_14:0_16:0)
TG(18:1_14:0_16:1)
TG(18:1e_14:0_18:1)
TG(18:2_14:0_15:0)
TG(18:2_14:0_16:0)
TG(18:2_15:0_16:0)
TG(18:2_15:0_16:1)
TG(18:2_16:0_18:0)
TG(18:2_16:0_24:0)
TG(18:2_16:1_18:1)
TG(18:3_14:0_16:0)
TG(18:3_16:0_16:1)
TG(20:0_16:0_16:1)
TG(22:5_12:3_12:4)
TG(30:0_14:0_14:0)
TG(30:1_18:2_18:2)
TG(36:2)
TG(4:0_6:0_20:5)
TG(40:2)
TG(40:6)
B
AcCa 24:1
C
AcCa 24:2
D
PC 36:4
E
PE 32:5
F
TG 18:3_16:0_16:1
G
TG 18:2_16:0_18:0
Normalized intensity
Esg-LexA>yki
PromE>Hnf4-i
H
# of branches
I
Tube area
J
Skeleton length
K
L
Arbitrary unit / area
pH3+ cells per midgut
Esg>
Luc-i
yki;Luc-i
yki;LpR1-i
yki;LpR2-i
Btf^ts >LpR1-i
Btf^ts >LpR2-i
M
N
O
P
Q
% of GFP+ region
Abdomen Area
Arbitary unit / area
ns

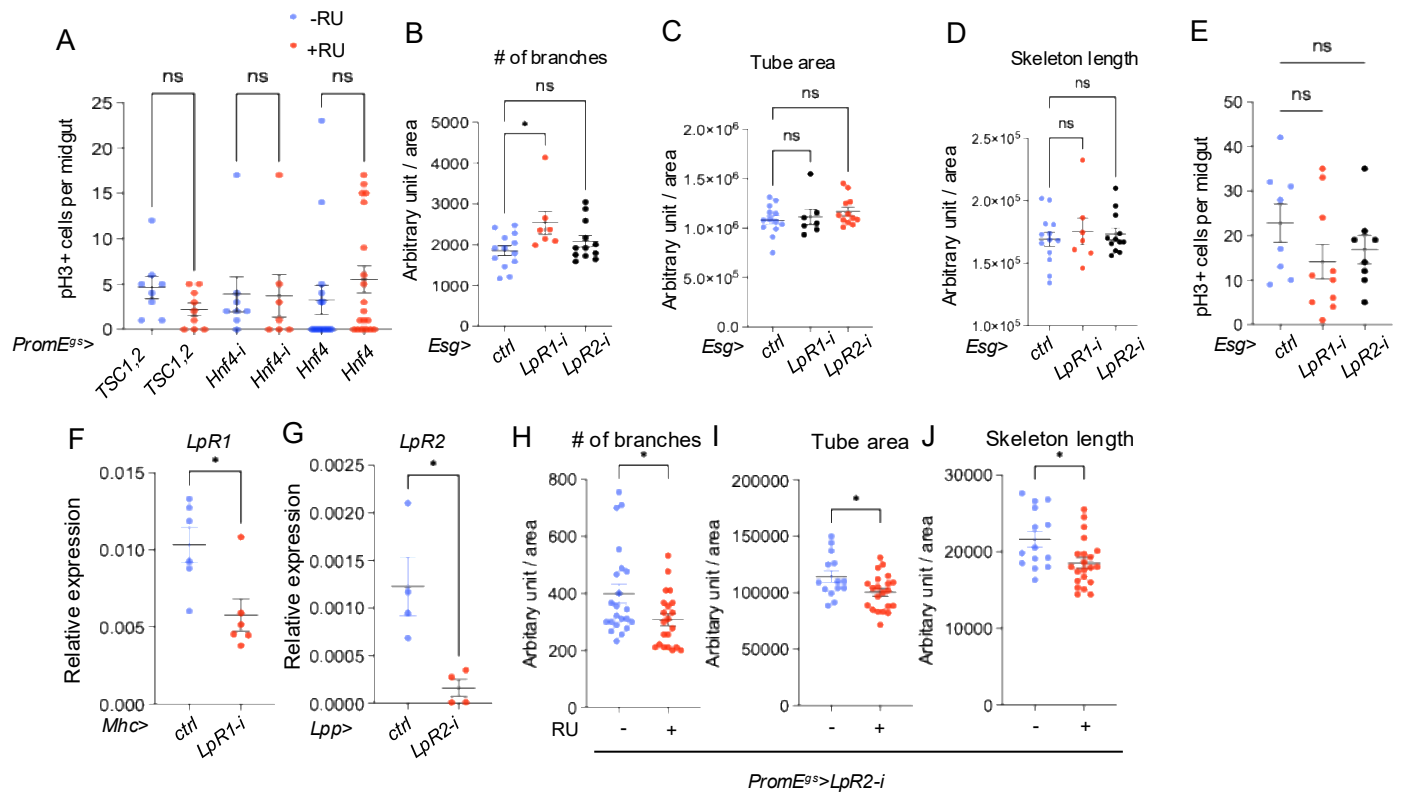
A
-RU
+RU
ns
ns
ns
pH3+ cells per midgut
25
20
15
10
5
0
PromEgs>
TSC1,2
TSC1,2
Hnf4-i
Hnf4-i
Hnf4
Hnf4
B
# of branches
ns
*
Arbitrary unit / area
5000
4000
3000
2000
1000
0
Esg>
ctrl
LpR1-i
LpR2-i
C
Tube area
ns
ns
Arbitrary unit / area
2.0×10^6
1.5×10^6
1.0×10^6
5.0×10^5
0.0
Esg>
ctrl
LpR1-i
LpR2-i
D
Skeleton length
ns
ns
Arbitrary unit / area
2.5×10^5
2.0×10^5
1.5×10^5
1.0×10^5
Esg>
ctrl
LpR1-i
LpR2-i
E
ns
ns
pH3+ cells per midgut
50
40
30
20
10
0
Esg>
ctrl
LpR1-i
LpR2-i
F
LpR1
*
Relative expression
0.015
0.010
0.005
0.000
Mhc>
ctrl
LpR1-i
G
LpR2
*
Relative expression
0.0025
0.0020
0.0015
0.0010
0.0005
0.0000
Lpp>
ctrl
LpR2-i
H
# of branches
*
Arbitary unit / area
800
600
400
200
0
RU
-
+
I
Tube area
*
Arbitary unit / area
200000
150000
100000
50000
0
-
+
J
Skeleton length
*
Arbitary unit / area
30000
20000
10000
0
-
+
PromEgs>LpR2-i

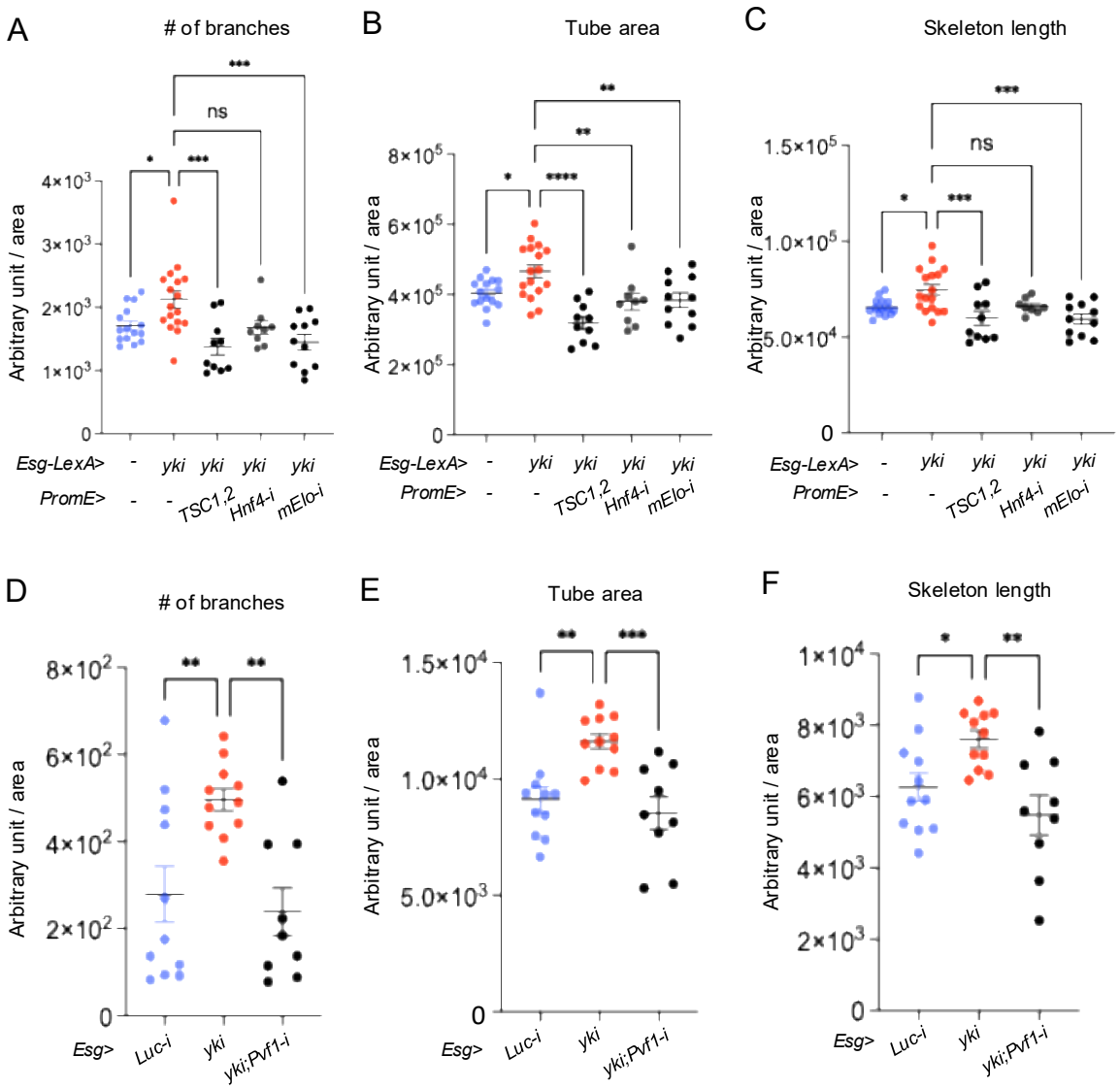
A
# of branches
Arbitrary unit / area
4×10^3
3×10^3
2×10^3
1×10^3
0
*
***
ns
***
Esg-LexA> - yki yki yki yki
PromE> - - TSC1,2 Hnf4-i mElo-i
B
Tube area
Arbitrary unit / area
8×10^5
6×10^5
4×10^5
2×10^5
0
*
****
**
**
Esg-LexA> - yki yki yki yki
PromE> - - TSC1,2 Hnf4-i mElo-i
C
Skeleton length
Arbitrary unit / area
1.5×10^5
1.0×10^5
5.0×10^4
0
*
***
ns
***
Esg-LexA> - yki yki yki yki
PromE> - - TSC1,2 Hnf4-i mElo-i
D
# of branches
Arbitrary unit / area
8×10^2
6×10^2
4×10^2
2×10^2
0
**
**
Esg> Luc-i yki yki;Pvf1-i
E
Tube area
Arbitrary unit / area
1.5×10^4
1.0×10^4
5.0×10^3
0
**
***
Esg> Luc-i yki yki;Pvf1-i
F
Skeleton length
Arbitrary unit / area
1×10^4
8×10^3
6×10^3
4×10^3
2×10^3
0
*
**
Esg> Luc-i yki yki;Pvf1-i

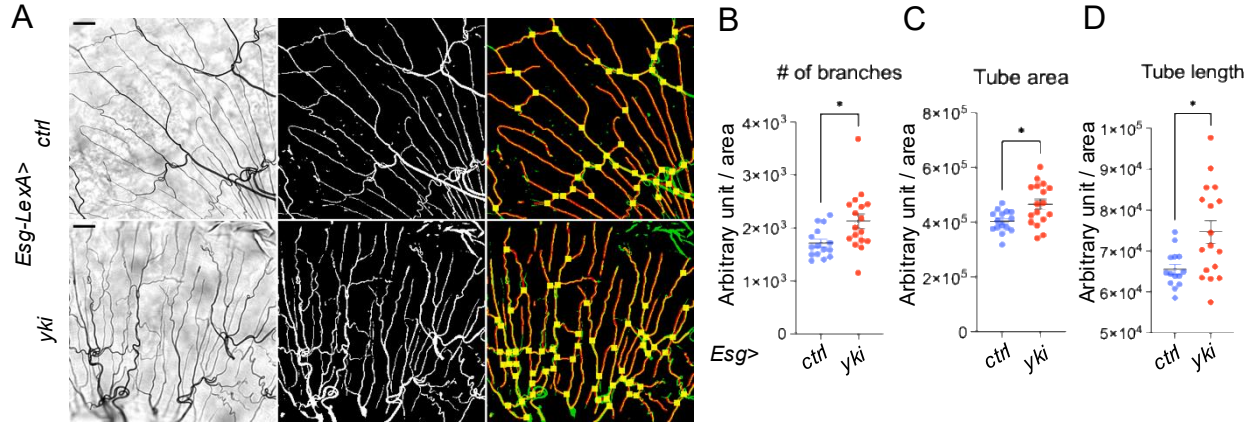
A
Esg-LexA>
ctrl
yki
B
# of branches
Arbitrary unit / area
4×10^3
3×10^3
2×10^3
1×10^3
0
*
Esg>
ctrl
yki
C
Tube area
Arbitrary unit / area
8×10^5
6×10^5
4×10^5
2×10^5
0
*
ctrl
yki
D
Tube length
Arbitrary unit / area
1×10^5
9×10^4
8×10^4
7×10^4
6×10^4
5×10^4
*
ctrl
yki

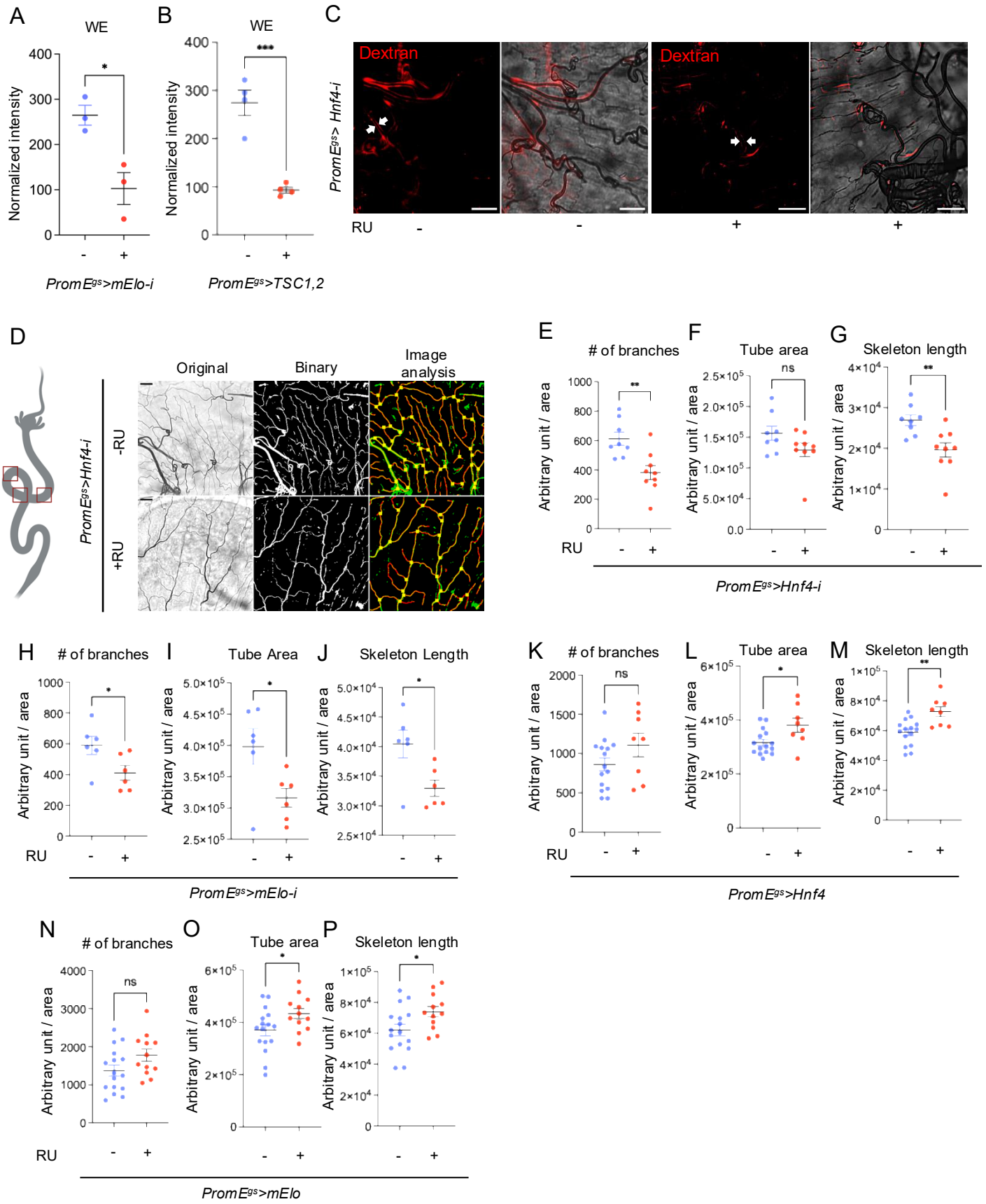
A
WE
Normalized intensity
400
300
200
100
0
*
-
+
PromEgs>mElo-i
B
WE
Normalized intensity
400
300
200
100
0
***
-
+
PromEgs>TSC1,2
C
Dextran
Dextran
PromEgs> Hnf4-i
RU
-
-
+
+
D
Original
Binary
Image analysis
PromEgs>Hnf4-i
-RU
+RU
E
# of branches
Arbitrary unit / area
1000
800
600
400
200
0
**
RU
-
+
F
Tube area
Arbitrary unit / area
2.5×10^5
2.0×10^5
1.5×10^5
1.0×10^5
5.0×10^4
0.0
ns
-
+
G
Skeleton length
Arbitrary unit / area
4×10^4
3×10^4
2×10^4
1×10^4
0
**
-
+
PromEgs>Hnf4-i
H
# of branches
Arbitrary unit / area
1000
800
600
400
200
0
*
RU
-
+
I
Tube Area
Arbitrary unit / area
5.0×10^5
4.5×10^5
4.0×10^5
3.5×10^5
3.0×10^5
2.5×10^5
*
-
+
J
Skeleton Length
Arbitrary unit / area
5.0×10^4
4.5×10^4
4.0×10^4
3.5×10^4
3.0×10^4
2.5×10^4
*
-
+
PromEgs>mElo-i
K
# of branches
Arbitrary unit / area
2000
1500
1000
500
0
ns
RU
-
+
L
Tube area
Arbitrary unit / area
6×10^5
4×10^5
2×10^5
0
*
-
+
M
Skeleton length
Arbitrary unit / area
1×10^5
8×10^4
6×10^4
4×10^4
2×10^4
0
**
-
+
PromEgs>Hnf4
N
# of branches
Arbitrary unit / area
4000
3000
2000
1000
0
ns
RU
-
+
O
Tube area
Arbitrary unit / area
6×10^5
4×10^5
2×10^5
0
*
-
+
P
Skeleton length
Arbitrary unit / area
1×10^5
8×10^4
6×10^4
4×10^4
2×10^4
0
*
-
+
PromEgs>mElo

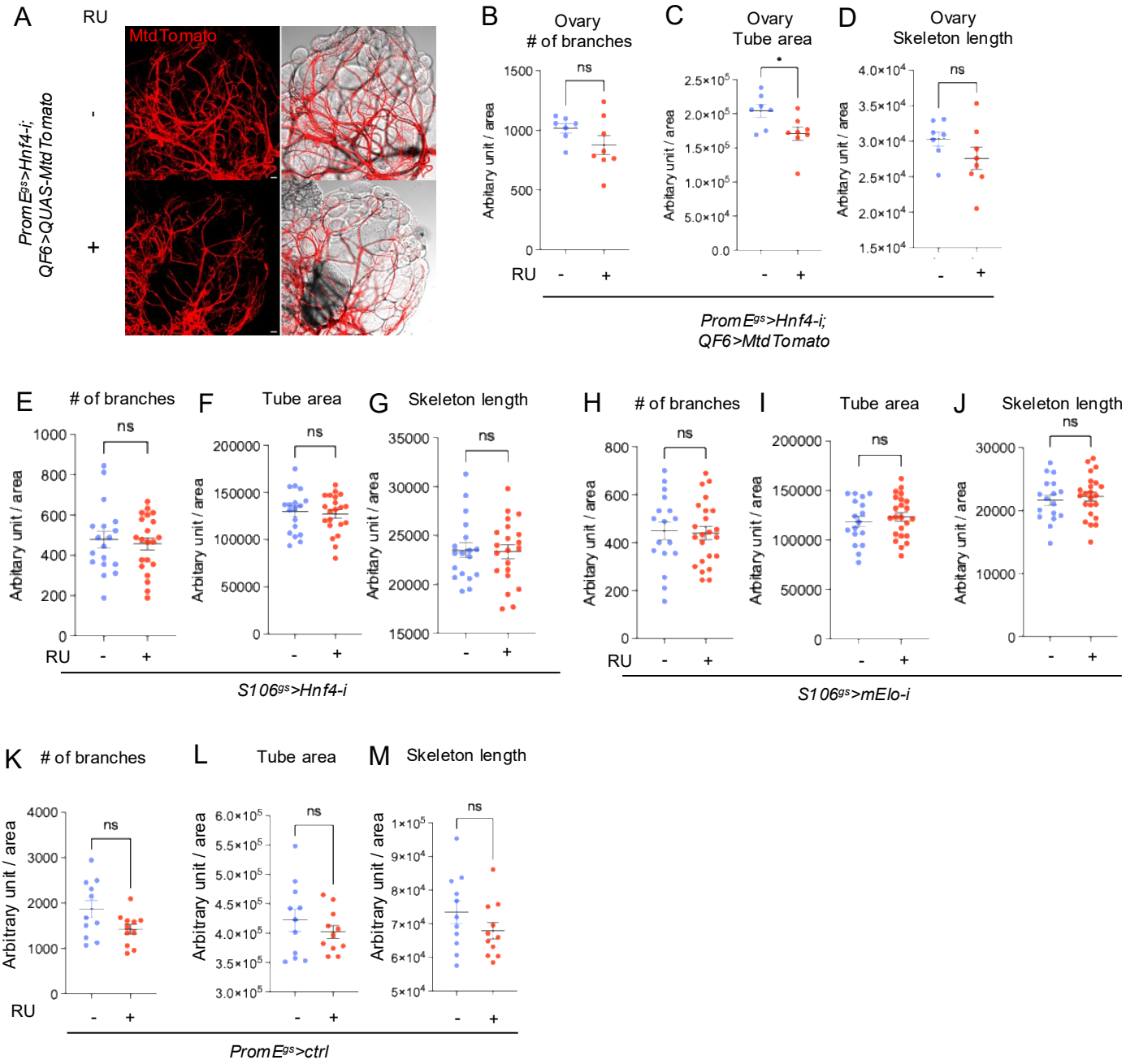
A
RU
MtdTomato
PromE^gs>Hnf4-i; QF6>QUAS-MtdTomato
-
+
B
Ovary
# of branches
C
Ovary
Tube area
D
Ovary
Skeleton length
Arbitary unit / area
ns
*
RU
PromE^gs>Hnf4-i; QF6>MtdTomato
E
# of branches
F
Tube area
G
Skeleton length
S106^gs>Hnf4-i
H
# of branches
I
Tube area
J
Skeleton length
S106^gs>mElo-i
K
# of branches
L
Tube area
M
Skeleton length
Arbitrary unit / area
PromE^gs>ctrl

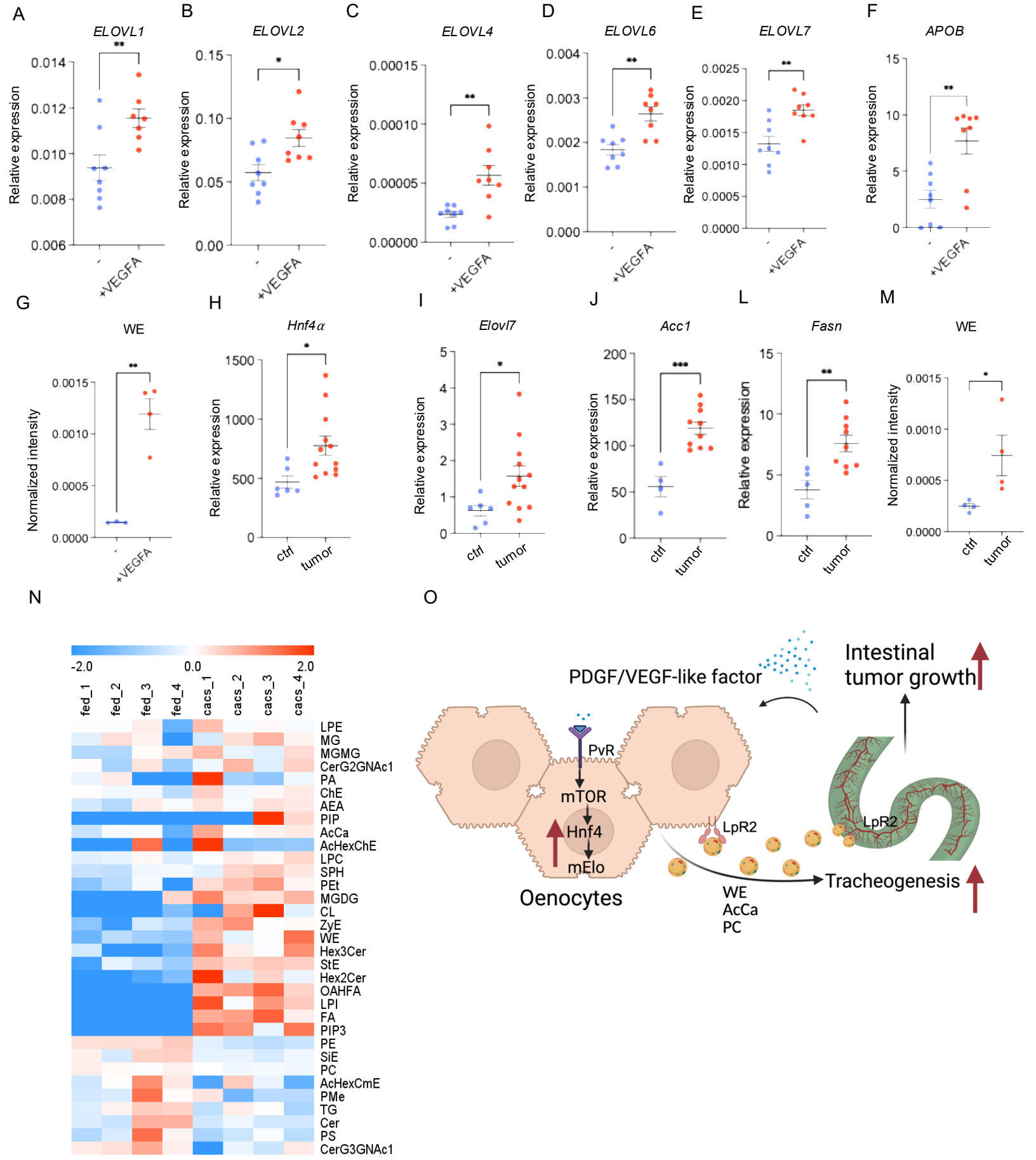
A
ELOVL1
Relative expression
0.014
0.012
0.010
0.008
0.006
**
-
+VEGFA
B
ELOVL2
Relative expression
0.15
0.10
0.05
0.00
*
-
+VEGFA
C
ELOVL4
Relative expression
0.00015
0.00010
0.00005
0.00000
**
-
+VEGFA
D
ELOVL6
Relative expression
0.004
0.003
0.002
0.001
0.000
**
-
+VEGFA
E
ELOVL7
Relative expression
0.0025
0.0020
0.0015
0.0010
0.0005
0.0000
**
-
+VEGFA
F
APOB
Relative expression
15
10
5
0
**
-
+VEGFA
G
WE
Normalized intensity
0.0015
0.0010
0.0005
0.0000
**
-
+VEGFA
H
Hnf4α
Relative expression
1500
1000
500
0
*
ctrl
tumor
I
Elovl7
Relative expression
5
4
3
2
1
0
*
ctrl
tumor
J
Acc1
Relative expression
200
150
100
50
0
***
ctrl
tumor
L
Fasn
Relative expression
15
10
5
0
**
ctrl
tumor
M
WE
Normalized intensity
0.0015
0.0010
0.0005
0.0000
*
ctrl
tumor
N
-2.0
0.0
2.0
fed_1
fed_2
fed_3
fed_4
cacs_1
cacs_2
cacs_3
cacs_4
LPE
MG
MGMG
CerG2GNAc1
PA
ChE
AEA
PIP
AcCa
AcHexChE
LPC
SPH
PEt
MGDG
CL
ZyE
WE
Hex3Cer
StE
Hex2Cer
OAHFA
LPI
FA
PIP3
PE
SiE
PC
AcHexCmE
PMe
TG
Cer
PS
CerG3GNAc1
O
PDGF/VEGF-like factor
Intestinal
tumor growth
PvR
mTOR
Hnf4
mElo
Oenocytes
LpR2
LpR2
WE
AcCa
PC
Tracheogenesis

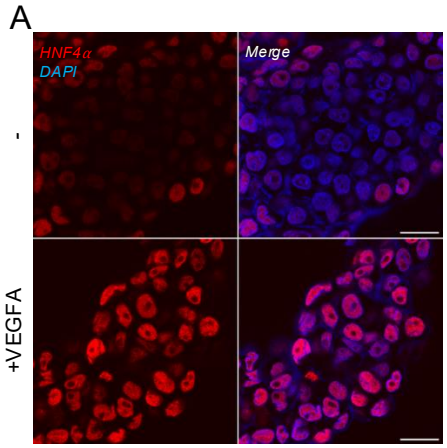
A
HNF4α
DAPI
Merge
-
+VEGFA

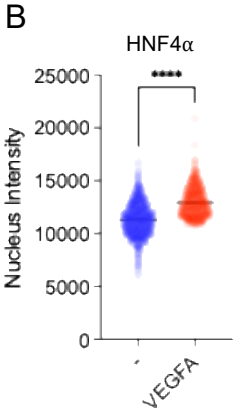
B
HNF4α
****
Nucleus Intensity
25000
20000
15000
10000
5000
0
-
VEGFA

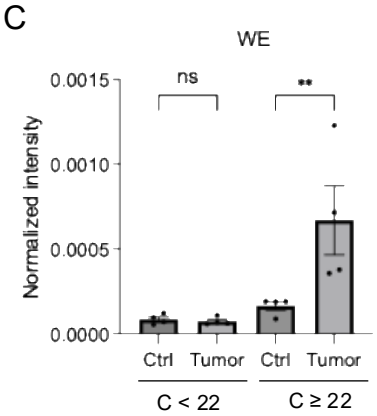
C
WE
ns
**
Normalized intensity
0.0015
0.0010
0.0005
0.0000
Ctrl
Tumor
Ctrl
Tumor
C < 22
C ≥ 22

D
-50.0
0.0
2.0
fed_1
fed_2
fed_3
fed_4
cacs_1
cacs_2
cacs_3
cacs_4